

X-RAY PROPERTIES OF THE FIRST SUNYAEV–ZEL'DOVICH EFFECT SELECTED GALAXY CLUSTER SAMPLE FROM THE SOUTH POLE TELESCOPE

K. ANDERSSON^{1,2}, B. A. BENSON^{3,4}, P. A. R. ADE⁵, K. A. AIRD⁶, B. ARMSTRONG⁷, M. BAUTZ¹, L. E. BLEEM^{3,8}, M. BRODWIN⁹, J. E. CARLSTROM^{3,4,8,10}, C. L. CHANG^{3,4}, T. M. CRAWFORD^{3,10}, A. T. CRITES^{3,10}, T. DE HAAN¹¹, S. DESAI⁷, M. A. DOBBS¹¹, J. P. DUDLEY¹¹, R. J. FOLEY⁹, W. R. FORMAN⁹, G. GARMIRE¹², E. M. GEORGE¹³, M. D. GLADDERS^{3,10}, N. W. HALVERSON¹⁴, F. W. HIGH¹⁵, G. P. HOLDER¹¹, W. L. HOLZAPFEL¹³, J. D. HRUBES⁶, C. JONES⁹, M. JOY¹⁶, R. KEISLER^{3,8}, L. KNOX¹⁷, A. T. LEE^{13,18}, E. M. LEITCH^{3,10}, M. LUEKER¹³, D. P. MARRONE^{3,6}, J. J. McMAHON^{3,4,19}, J. MEHL^{3,10}, S. S. MEYER^{3,4,8,10}, J. J. MOHR^{2,20,21}, T. E. MONTROY²², S. S. MURRAY⁹, S. PADIN^{3,10}, T. PLAGGE^{10,13}, C. PRYKE^{3,4,10}, C. L. REICHARDT¹³, A. REST¹⁵, J. RUEL¹⁵, J. E. RUHL²², K. K. SCHAFER^{3,4}, L. SHAW^{11,23}, E. SHIROKOFF¹³, J. SONG⁷, H. G. SPIELER¹⁸, B. STALDER⁹, Z. STANISZEWSKI²², A. A. STARK⁹, C. W. STUBBS^{9,15}, K. VANDERLINDE¹¹, J. D. VIEIRA^{3,8,24}, A. VIKHLINEV^{9,25}, R. WILLIAMSON^{3,10}, Y. YANG⁷, O. ZAHN¹³, AND A. ZENTENO^{2,20}

¹ MIT Kavli Institute for Astrophysics and Space Research, Massachusetts Institute of Technology,
 77 Massachusetts Avenue, Cambridge, MA 02139, USA; kanderss@space.mit.edu

² Department of Physics, Ludwig-Maximilians-Universität, Scheinerstr. 1, 81679 München, Germany

³ Kavli Institute for Cosmological Physics, University of Chicago, 5640 South Ellis Avenue, Chicago, IL 60637, USA

⁴ Enrico Fermi Institute, University of Chicago, 5640 South Ellis Avenue, Chicago, IL 60637, USA

⁵ Department of Physics and Astronomy, Cardiff University, CF24 3YB, UK

⁶ Department of Astronomy and Astrophysics, University of Chicago, 5640 South Ellis Avenue, Chicago, IL 60637, USA

⁷ Department of Astronomy, University of Illinois, 1002 West Green Street, Urbana, IL 61801, USA

⁸ Department of Physics, University of Chicago, 5640 South Ellis Avenue, Chicago, IL 60637, USA

⁹ Harvard-Smithsonian Center for Astrophysics, 60 Garden Street, Cambridge, MA 02138, USA

¹⁰ Department of Astronomy and Astrophysics, University of Chicago, 5640 South Ellis Avenue, Chicago, IL 60637, USA

¹¹ Department of Physics, McGill University, 3600 Rue University, Montreal, Quebec H3A 2T8, Canada

¹² Department of Astronomy and Astrophysics, Pennsylvania State University, 525 Davey Lab, University Park, PA 16802, USA

¹³ Department of Physics, University of California, Berkeley, CA 94720, USA

¹⁴ Department of Astrophysical and Planetary Sciences and Department of Physics, University of Colorado, Boulder, CO 80309, USA

¹⁵ Department of Physics, Harvard University, 17 Oxford Street, Cambridge, MA 02138, USA

¹⁶ Department of Space Science, VP62, NASA Marshall Space Flight Center, Huntsville, AL 35812, USA

¹⁷ Department of Physics, University of California, One Shields Avenue, Davis, CA 95616, USA

¹⁸ Physics Division, Lawrence Berkeley National Laboratory, Berkeley, CA 94720, USA

¹⁹ Department of Physics, University of Michigan, 450 Church Street, Ann Arbor, MI 48109, USA

²⁰ Excellence Cluster Universe, Boltzmannstr. 2, 85748 Garching, Germany

²¹ Max-Planck-Institut für extraterrestrische Physik, Giessenbachstr. 85748 Garching, Germany

²² Physics Department and CERCA, Case Western Reserve University, 10900 Euclid Ave., Cleveland, OH 44106, USA

²³ Department of Physics, Yale University, P.O. Box 208210, New Haven, CT 06520-8120, USA

²⁴ California Institute of Technology, Pasadena, CA 91125, USA

²⁵ Space Research Institute (IKI), Profsoyuznaya 84/32, Moscow, Russia

Received 2010 June 17; accepted 2011 May 23; published 2011 August 11

ABSTRACT

We present results of X-ray observations of a sample of 15 clusters selected via their imprint on the cosmic microwave background from the thermal Sunyaev–Zel'dovich (SZ) effect. These clusters are a subset of the first SZ-selected cluster catalog, obtained from observations of 178 deg² of sky surveyed by the South Pole Telescope (SPT). Using X-ray observations with *Chandra* and *XMM-Newton*, we estimate the temperature, T_X , and mass, M_g , of the intracluster medium within r_{500} for each cluster. From these, we calculate $Y_X = M_g T_X$ and estimate the total cluster mass using an M_{500} – Y_X scaling relation measured from previous X-ray studies. The integrated Comptonization, Y_{SZ} , is derived from the SZ measurements, using additional information from the X-ray-measured gas density profiles and a universal temperature profile. We calculate scaling relations between the X-ray and SZ observables and find results generally consistent with other measurements and the expectations from simple self-similar behavior. Specifically, we fit a $Y_{\text{SZ}}\text{--}Y_X$ relation and find a normalization of 0.82 ± 0.07 , marginally consistent with the predicted ratio of $Y_{\text{SZ}}/Y_X = 0.91 \pm 0.01$ that would be expected from the density and temperature models used in this work. Using the Y_X -derived mass estimates, we fit a $Y_{\text{SZ}}\text{--}M_{500}$ relation and find a slope consistent with the self-similar expectation of $Y_{\text{SZ}} \propto M^{5/3}$ with a normalization consistent with predictions from other X-ray studies. We find that the SZ mass estimates, derived from cosmological simulations of the SPT survey, are lower by a factor of 0.78 ± 0.06 relative to the X-ray mass estimates. This offset is at a level of 1.3σ when considering the $\sim 15\%$ systematic uncertainty for the simulation-based SZ masses. Overall, the X-ray measurements confirm that the scaling relations of the SZ-selected clusters are consistent with the properties of other X-ray-selected samples of massive clusters, even allowing for the broad redshift range ($0.29 < z < 1.08$) of the sample.

Key words: galaxies: clusters: intracluster medium – X-rays: galaxies: clusters

1. INTRODUCTION

Large-area cluster surveys extending to high redshift can be used to study the evolution of the abundance of galaxy clusters, thereby delivering precise constraints on the amount and nature of the dark energy (Wang & Steinhardt 1998; Haiman et al. 2001). The accuracy with which the observed mass proxy can be linked to the true cluster mass fundamentally limits the cosmological constraints from the survey. In particular, a redshift-dependent bias on a survey’s cluster mass estimates could mimic a time-evolving dark energy, so this systematic must be understood and constrained. Clusters are known to evolve—through mergers, galaxy and star formation, and variable contributions from active galactic nuclei (AGNs)—and these effects will influence the evolution of any cluster observable at some level.

Most of the baryonic mass in clusters is in the form of an intracluster gas that can be heated to several keV as it virializes in a massive cluster’s gravitational potential well. This gas is visible in the X-ray band via thermal bremsstrahlung and also from its distortion of the cosmic microwave background (CMB) from inverse Compton scattering, otherwise known as the Sunyaev–Zel’dovich (SZ) effect (Sunyaev & Zeldovich 1972). The lowest scatter cluster observables that scale with cluster mass, M , are likely those most closely related to the gas pressure (e.g., Kravtsov et al. 2006) and hence related to the total energy of the gas. The SZ intensity is proportional to the Comptonization, the line-of-sight integral of the gas pressure. Hence, the SZ signal integrated over the cluster’s extent, Y_{SZ} , measures the total pressure in the cluster. An X-ray analog, Y_X , can be constructed from the product of the cluster’s total gas mass and the X-ray spectroscopic temperature (Kravtsov et al. 2006).

The intrinsic scatter in the $M-Y_X$ relation has been found to be smaller than the measurement error in X-ray studies conducted to date (Vikhlinin et al. 2006, 2009a; Sun et al. 2009) and has been used to place interesting constraints on the dark energy equation of state with only a relatively small sample of clusters (Vikhlinin et al. 2009b). The slope and scatter of the relationship between Y_{SZ} and the cluster mass, M , has been studied extensively in simulations and is expected to be relatively insensitive to non-gravitational physics (Nagai 2006), the dynamical state of clusters (Jeltema et al. 2008), and the presence of cool cores (Motl et al. 2005). The expected close correlation between cluster mass and Y_{SZ} , as well as the redshift independence of the SZ brightness, strongly motivates using SZ cluster surveys for cosmological studies (Carlstrom et al. 2002).

Recently, there has been significant progress in measuring the SZ signal from clusters. High-resolution imaging has been obtained for single objects (e.g., Nord et al. 2009; Mason et al. 2010) and intracluster medium (ICM) profiles have been measured for moderately sized samples (e.g., Mroczkowski et al. 2009; Plagge et al. 2010). The first clusters discovered with a blind SZ survey were reported in Staniszewski et al. (2009) and showed the capability of the SZ signal as a cluster finder. From larger samples, scaling relations have been measured between the SZ signal and mass estimates from both X-ray and weak lensing measurements (e.g., Bonamente et al. 2008; Marrone et al. 2009; Melin et al. 2011). Notably, Melin et al. (2011) measured a $Y_{\text{SZ}}-M$ relation from binned *Wilkinson Microwave Anisotropy Probe* (*WMAP*) fluxes at the location of known X-ray-selected clusters combined with X-ray luminosity-based mass estimates. They found a $Y_{\text{SZ}}-M$ relation with a normalization and slope that matched the X-ray prediction, however similar analyses

have found conflicting results (Komatsu et al. 2011). More detailed observations comparing SZ and X-ray measurements will improve our understanding of the gas pressure in clusters.

The first SZ-selected catalog of clusters was presented in Vanderlinde et al. (2010, hereafter V10) and included the first meaningful cosmological constraints from an SZ cluster survey. In V10, the sample of 21 clusters had a median redshift of $z = 0.74$ and was predicted to be 100% complete above a mass threshold of $M_{500} \approx 3 \times 10^{14} h^{-1} M_{\odot}$ at $z > 0.6$. The cosmological constraints from V10 were limited by uncertainties in the cluster mass calibration. This calibration relied on the dark matter simulations of Shaw et al. (2009), with gas physics based on the models in Bode et al. (2007), to link the SZ significance to cluster mass. This introduced a $\sim 15\%$ systematic uncertainty in the mass calibration due to uncertainties in the pressure normalization of the simulations. Therefore, an important first step to improve the cosmological constraints of V10 is to tie the SZ observables to observationally calibrated X-ray scaling relations, such as those in Vikhlinin et al. (2009a). The V10 cluster sample is also unique because of its high median redshift and SZ selection. X-ray observations of these clusters could allow additional constraints on the redshift evolution of X-ray scaling relations, which typically have been studied from X-ray-selected samples concentrated at $z < 0.6$ (e.g., Maughan 2007; Vikhlinin et al. 2009a; Mantz et al. 2010).

In this work, we present results from X-ray observations of a subset of 15 clusters with the highest SZ significance from V10. We report on the X-ray observables of this sample and use X-ray scaling relations from Vikhlinin et al. (2009a) to estimate each cluster’s mass. For each cluster, we also note details of the cluster’s X-ray morphology and the identification of X-ray sources with objects in other catalogs. We use the X-ray measured gas density profiles to improve the SZ estimates of integrated Comptonization, Y_{SZ} . Finally, we construct X-ray and SZ scaling relations, specifically the $Y_{\text{SZ}}-Y_X$ and $Y_{\text{SZ}}-M_{500}$ relations, and compare these relations to expectations and other results.

The paper is organized as follows. Section 2 describes the cluster sample and the SZ, optical and X-ray observations. Section 3 discusses the X-ray data analysis, the estimation of gas mass and temperature while Section 4 describes the estimate of gravitational mass. In Section 5, we discuss the analysis of the South Pole Telescope (SPT) data and deprojection of the SZ measurements. In Section 6, the X-ray and SZ scaling relations are investigated and we conclude with a discussion in Section 7. The properties of individual clusters are discussed in the Appendix.

In all calculations, we have assumed a *WMAP7+BAO+ H_0* Λ CDM cosmology (Komatsu et al. 2011) with $\Omega_M = 0.272$, $\Omega_{\Lambda} = 0.728$, and $H_0 = 70.2 \text{ km s}^{-1} \text{ Mpc}^{-1}$ with distance measurements from baryon acoustic oscillations (BAOs) in the distribution of galaxies (Percival et al. 2010) and the Hubble constant (H_0) measurement from Riess et al. (2009). Everywhere, we define M_{500} as the mass inside r_{500} , within which the matter density is 500 times the critical density at the cluster redshift, $\rho_{\text{crit}}(z) = 3H^2(z)/8\pi G$, where $H(z)$ is the Hubble parameter.

2. CLUSTER SAMPLE AND OBSERVATIONS

The clusters used in this work were selected from an SZ detection significance limited catalog from the SPT cluster survey described in V10. For all clusters, we performed follow-up optical imaging to identify galaxy cluster counterparts and measure

redshifts (High et al. 2010). Sixteen cluster candidates with SZ detection significance above 5.4 were selected for X-ray follow-up with *Chandra* and *XMM-Newton*. One candidate was later discovered to be a spurious detection and is discussed in more detail in the Appendix. This section briefly describes the SZ, optical, and X-ray data sets.

2.1. SPT SZ Observations and the Cluster Sample

The 10 m diameter SPT is a millimeter wavelength telescope located at the South Pole. Its primary science goal is to conduct a $\sim 2000 \text{ deg}^2$ survey to find clusters of galaxies via measurements of the SZ effect. The receiver consists of a 960 element bolometer array that is sensitive in three frequency bands centered at 95, 150, and 220 GHz. In this work, we only use observations at 150 GHz, the SPT frequency band with the most SZ sensitivity. Details of the telescope and receiver can be found in Padin et al. (2008) and Carlstrom et al. (2011).

In 2008, the SPT surveyed two $\sim 100 \text{ deg}^2$ regions. These two fields are approximately square on the sky and centered at right ascension (R.A.) $5^{\text{h}}30^{\text{m}}$, declination (decl.) -55° and R.A. $23^{\text{h}}30^{\text{m}}$, decl. -55° . The data from the first of these fields were used to report the first SZ-discovered clusters (Staniszewski et al. 2009), to measure source counts of extragalactic millimeter-wavelength emitting objects (Vieira et al. 2010), and to measure small-scale temperature anisotropies due to the SZ effect from unresolved clusters and emission from point sources (Lueker et al. 2010; Hall et al. 2010). In V10, the data from both fields were used to report the first SZ detection significance limited catalog of 22 cluster candidates.

The SZ observations, data processing, and mapmaking used in this work are described in detail in V10, and only a brief overview is provided here. Each field was scanned in azimuth at a constant velocity, with the scans stepped in elevation. With the velocity and elevation step used, it takes ~ 2 hr to cover an entire 100 deg^2 field. This scan is then repeated several hundred times to decrease the noise in the co-added map. Each detector timestamp is filtered to remove both long timescale drifts and sky signal that is spatially correlated across the focal plane. The filtering effectively acts as a high pass filter; the filter used for the SZ cluster analysis removes signal on spatial scales larger than $\sim 0.5'$. The data are combined to make a map by reconstructing the pointing for each detector and then averaging the data from all the detectors using inverse-variance weighting. The 150 GHz maps were calibrated to an accuracy of 3.6% by direct comparison to the *WMAP* 5 year maps (Lueker et al. 2010). The final map of each field has a sensitivity limit of $18 \mu\text{K arcmin}$.

Cluster candidates were identified in the SPT maps by using a matched spatial filter technique (Haehnelt & Tegmark 1996; Melin et al. 2006). Here we summarize the method and results as used in V10. The SPT maps consist of several sources of signal, including primary CMB anisotropy, unresolved point sources, and SZ signal from clusters. To identify cluster candidates, the SPT maps are filtered in Fourier space to give more weighting to signals matching the expected spatial scales of clusters. Twelve different spatial filters were constructed using spherical β -models with β fixed to 1 and core radii evenly spaced between 0.25 and 3.0. With these, the SPT maps were filtered and cluster candidates were identified as decrements in the filtered map. The significance of a candidate was quantified by their signal relative to the standard deviation in the filtered map or signal to noise (S/N). For a given cluster candidate, the highest S/N across all filter scales was defined as ξ . To avoid spurious identifications

Table 1
Chandra and *XMM-Newton* Observation IDs

Name	Observation ID
SPT-CL J0000-5748	9335
SPT-CL J0509-5342	9432
SPT-CL J0516-5430	9331
SPT-CL J0528-5300	9341, 10862, 11996
SPT-CL J0533-5005	11748, 12001
SPT-CL J0546-5345	9332, 9336, 10851, 10864
SPT-CL J0551-5709	11871
SPT-CL J0559-5249	0604010301
SPT-CL J2331-5051	9333, 11738
SPT-CL J2332-5358	0604010101
SPT-CL J2337-5942	11859
SPT-CL J2341-5119	9345
SPT-CL J2342-5411	11741, 11870, 12014
SPT-CL J2355-5056	11746, 11998
SPT-CL J2359-5009	9334, 11742, 11864

Notes. Ten-digit numbers refer to *XMM-Newton* observation IDs, ≤ 5 digit numbers are *Chandra* IDs.

from ringing around spatially filtered bright point sources, a $4'$ radius region around all 5σ positive sources was masked before spatial filtering. The total sky area used in both fields after masking was 178 deg^2 . Further details of the SZ analysis relevant to the results presented here are given in Section 5.

The 16 cluster candidates with the largest ξ were selected for X-ray follow-up with the *Chandra* and *XMM-Newton* X-ray telescopes. The original candidate list was based on a similar, but earlier version of the list that appeared in V10. This change reordered the list somewhat, such that 16 of the 17 most significant candidates from V10 had X-ray follow-up. In Table 1 we list the *Chandra* and *XMM-Newton* observation IDs used, while in Table 2 we give the position and ξ from V10 for the 15 confirmed clusters with X-ray observations. One of the candidates with X-ray follow-up, SPT-CL J2343-5521, is not listed because it is very likely a false detection. Its X-ray observation is discussed further in the Appendix.

2.2. Optical Imaging and Spectroscopy

Optical counterparts for the clusters selected by SZ detection significance were identified and photometric redshifts were measured via a combination of imaging from the Blanco Cosmology Survey (BCS) and targeted observations using the Magellan telescopes. For a subset of clusters, spectroscopic redshifts were also obtained. Further details of the optical data and analysis can be found in High et al. (2010) and are briefly described below.

The BCS is an optical survey of two $\sim 50 \text{ deg}^2$ fields that lie inside the two 2008 SPT fields described in Section 2.1. BCS used the Mosaic-II wide field imager on the Blanco 4 m telescope at the Cerro Tololo Inter-American Observatory in Chile. The BCS obtained contiguous deep optical imaging in the *griz* bands across their survey fields, and these data have been processed using a development version of the DES data management system (Ngeow et al. 2006; Mohr et al. 2008) and then used in the study of the galaxy population and in the redshift estimation of the first SPT survey fields (Ngeow et al. 2009; Staniszewski et al. 2009; High et al. 2010; Brodwin et al. 2010; Zenteno et al. 2011). These data are publicly available through the NOAO Survey Program and have been used by other groups to study clusters in the SPT survey region (Menanteau et al. 2009, 2010; Menanteau & Hughes 2009; McInnes et al.

Table 2
Chandra and XMM-Newton Observations

Name	R.A. ^a	Decl. ^a	ξ ^b	Photo- ^c z	Spec- ^c z	Exposure (ks)	Sourced Counts	n_{H} ^e (10^{20} cm $^{-2}$)	$d_{X-\text{SZ}}$ ^f '	Merger?
SPT-CL J0000-5748	0.25	-57.807	5.48	0.74	...	28.1	1451	1.37	0.16	
SPT-CL J0509-5342	77.336	-53.705	6.61	0.47	0.4626	27.3	2441	1.46	0.13	✓
SPT-CL J0516-5430	79.148	-54.506	9.42	0.25	0.2952 ^g	8.4	2136	2.05	0.15	✓
SPT-CL J0528-5300	82.017	-53.0	5.45	0.75	0.7648	36.5	356	3.23	0.20	
SPT-CL J0533-5005	83.398	-50.092	5.59	0.83	0.8810	41.5	201	2.95	0.53	✓
SPT-CL J0546-5345	86.654	-53.761	7.69	1.16	1.0665 ^h	55.6	1304	6.78	0.13	✓
SPT-CL J0551-5709	87.902	-57.156	6.13	0.41	0.4230	19.8	876	6.27	0.53	✓
SPT-CL J0559-5249 ^X	89.925	-52.826	9.28	0.66	0.6112	42.0	2006	5.08	0.42	✓
SPT-CL J2331-5051	352.958	-50.864	8.04	0.55	0.5707	34.2	2428	1.12	0.23	✓
SPT-CL J2332-5358 ^{X,i}	353.109	-53.976	13.05	0.32	...	18.9	4826	1.28	0.36	
SPT-CL J2337-5942	354.354	-59.705	14.94	0.77	0.7814	19.8	1488	1.45	0.12	✓
SPT-CL J2341-5119	355.299	-51.333	9.65	1.03	0.9983	79.0	2090	1.21	0.26	
SPT-CL J2342-5411	355.69	-54.189	6.18	1.08	...	133.7	1193	1.49	0.23	
SPT-CL J2355-5056	358.955	-50.937	5.89	0.35	...	20.6	1798	1.27	0.61	
SPT-CL J2359-5009	359.921	-50.16	6.35	0.76	...	57.9	713	1.33	0.78	✓

Notes.^X*XMM-Newton* observation. The listed exposure times and source counts are for MOS1, MOS2, and PN combined.^a R.A. and decl. determined from the SPT detection.^b Signal-to-noise measured in 150 GHz SPT maps as described in V10.^c Listed photometric and spectroscopic redshifts are based on analysis in High et al. (2010).^d Based on *Chandra/XMM-Newton* count rate in the 0.5–7.0 keV band, within $0.5 r_{500}$.^e Hydrogen column density from the Leiden–Argentine–Bonn survey (Kalberla et al. 2005).^f Distance between SPT detection and X-ray centroid.^g Spectroscopic redshift from the REFLEX cluster survey (Böhringer et al. 2004).^h Spectroscopic redshift from (Brodwin et al. 2010).ⁱ The position and ξ of this cluster are modified from V10 after correcting for the effects of a point-source coincident with the cluster, as described in Section 5.4.

2009; Šuhada et al. 2010). For the nine clusters outside the BCS fields, optical imaging in the *griz* bands was obtained with the Inamori Magellan Areal Camera and Spectrograph (IMACS; Dressler et al. 2006) on the Magellan Baade 6.5 m telescope in Las Campanas, Chile. Five cluster candidates in the BCS fields were also re-observed with Magellan. In contrast to BCS, the Magellan observations were performed adaptively, where the candidates were observed in \sim 100 s increments until the galaxy cluster was detected.

Optical counterparts of each SPT candidate were identified by searching for red sequence objects within a 2' radius of the SPT candidate location. A cluster was identified through an excess of red sequence objects relative to the background, and the photometric redshift was estimated by fitting a red sequence model. The redshift uncertainty varies over the sample, however they are typically $\Delta z \sim 0.03$ and can be as large as $\Delta z = 0.10$ for clusters at $z \sim 1$ (see High et al. 2010 for details).

For 8 of 16 cluster candidates, spectroscopic measurements were obtained using the Low Dispersion Survey Spectrograph (LDSS3) on the Magellan Clay 6.5 m telescope. These observations are described in High et al. (2010). For one candidate, SPT-CL J0546-5345, multislit spectroscopy was done with IMACS on the Magellan Baade 6.5 m telescope (Brodwin et al. 2010). The spectroscopic targets were chosen to span the redshift range of the sample to help calibrate the photometric redshifts. One cluster, SPT-CL J0516-5430, has a previous spectroscopic redshift from the REFLEX cluster survey (Böhringer et al. 2004). In Table 2, we give the photometric redshifts for each of the 15 clusters included in this work and the spectroscopic redshift where available.

2.3. Chandra and XMM-Newton Observations

As described in Section 2.1, the 16 cluster candidates with the highest detection significance, ξ , were selected for an X-ray follow-up program. This program was split between several observing cycles and proposals between the *Chandra* and *XMM-Newton* X-ray satellites.

In the original planning of X-ray observations, the observing time required for each cluster was estimated from preliminary predictions of the SZ-significance-to-mass relation and a mass–luminosity scaling. The uncertainty in the relations does not allow an accurate estimate of the exposure needed for a required number of photons. The estimates were informed by *ROSAT* fluxes where available. For clusters scheduled for multiple observations with *Chandra*, the integration time was modified accordingly once a flux had been measured.

To date, the *Chandra* program consists of two GTO programs in AO-9 (295 ks, total), two GTO programs in AO-11 (340 ks, total), and a GO program in AO-11 (310 ks). When completed, the *Chandra* program will have collected at least 1500 cluster photons within $0.5 r_{500}$ and in the 0.5–7.0 keV energy band for each of 12 clusters in the sample. This limit was chosen to enable measuring of the ICM temperature, T_X , to 15% accuracy. For one very faint object, SPT-CL J0553-5005, the data will not be sufficient to measure the temperature to this accuracy in the current program. The *Chandra* ACIS-I count rate in the 0.5–7.0 keV band for this object is only 0.005 counts s $^{-1}$.

Four of the candidates have been observed with *XMM-Newton*, one of which is an archival observation (SPT-CL J0516-5430, also RXCJ0516.7-5430); the other three are from a 2008 program (SPT-CL J0559-5249, SPT-CL J2332-5358, and

SPT-CL J2337-5942). All of these observations have more than the required 1500 counts. For two of the clusters, there exists both *Chandra* and *XMM-Newton* data (SPT-CL J0516-5430 and SPT-CL J2337-5942) and these are all analyzed in this work. We chose to re-observe these two clusters with *Chandra* to better identify and remove X-ray point sources in the analysis. The low redshift and high mass of the clusters made these observations possible with a comparably small amount of observing time.

While we find consistent results from the analysis of data from the two different satellites, we choose to use the *Chandra* data for the two clusters with data from both instruments since both the high spatial resolution and stable background of *Chandra* are desirable. For the two clusters where only *XMM-Newton* data were available, we derive our results from these data using the methods as described below.

X-ray measurements of SPT-CL J2332-5358 and SPT-CL J2342-5411 were also reported by Šuhada et al. (2010) from the *XMM-BCS* survey. These measurements were not as deep as the observations discussed in our work, however we find X-ray observables consistent with their measurements.

Currently, there are eight out of the 15 clusters for which the required 1500 source counts have not yet been collected with either instrument. However, we include these in the analysis since the existing data provide useful constraints.

3. X-RAY DATA ANALYSIS

3.1. Data Reduction

The exposure times and resulting source counts from the *Chandra* and *XMM-Newton* observations are listed in Table 2. We also list the cluster coordinates and SZ S/N as described in V10 as well as the optical redshifts and the galactic absorbing hydrogen column from the Leiden–Argentine–Bonn survey (Kalberla et al. 2005). Source counts are quoted within $0.5 r_{500}$ which is estimated from the Y_X parameter and the $M_{500}-Y_X$ relation (see Section 3.5).

The *Chandra* data were reduced using CIAO 4.1 and CALDB 4.1.3. All data were taken with the ACIS-I nominal aim point in VFAINT telemetry mode and additional screening to reject particle background was applied. To remove periods of flaring background, we extracted point-source-subtracted light curves in the 0.3–12 keV band and filtered these using a 3σ threshold. *XMM-Newton* data were reduced using SAS 9.0 and reprocessed. Source-free light curves were generated in hard (MOS:10–12 keV, pn:12–14 keV) and soft (MOS:0.3–10 keV, pn:0.3–10 keV) energy bands separately and a 3σ cut was applied to remove periods of high background.

3.2. Data Analysis Methods

For the X-ray observables, T_X , M_g , and Y_X we use scaling relations from Vikhlinin et al. (2009a) iteratively to determine the r_{500} radius where the observable is measured.

The r_{500} radii used for the measurement of T_X were estimated using the $M-T_X$ relation in Vikhlinin et al. (2009a) from samples of local clusters with deep exposures for which hydrostatic masses could be determined:

$$M_{500} = (3.02 \pm 0.11)10^{14} h^{-1} M_\odot \\ \times \left(\frac{kT}{5 \text{ keV}} \right)^{(1.53 \pm 0.08)} E(z)^{-1}, \quad (1)$$

where

$$E(z) = H(z)/H_0 \\ = \sqrt{(1+z)^2(1+\Omega_M z) - z(2+z)\Omega_\Lambda}. \quad (2)$$

The radius is then defined as

$$r_{500} = \left(\frac{3M_{500}}{4\pi 500 \rho_{\text{crit}}(z)} \right)^{1/3}. \quad (3)$$

Similarly, in the estimation of the gas mass, M_g , described below, we use the gas-fraction relation

$$f_{g,500} = (0.0764 \pm 0.004)h^{-1.5} \\ + (0.0225 \pm 0.004)h^{-1.5} \log M_{15}, \quad (4)$$

where $f_{g,500}$ is the gas mass fraction within r_{500} , $f_{g,500} = M_g/M_{500}$, and M_{15} is the total mass, M_{500} , in units of $10^{15} h^{-1} M_\odot$.²⁶ With this relation we explicitly take into account the observed trend of $f_{g,500}$ with cluster mass (e.g., Vikhlinin et al. 2009a). The gas mass estimation is much more dependent on the aperture radius than the estimate of temperature and M_g must be estimated iteratively to obtain a self-consistent result. Given a gas mass, we use Equation (4) to determine the total mass and, hence, r_{500} .

For the estimation of the $Y_X = M_g \times T_X$ parameter, we analogously estimate the aperture radius through the determination of

$$M_{500} = (5.77 \pm 0.20)10^{14} h^{1/2} M_\odot \\ \times \left(\frac{Y_X}{3 \times 10^{14} M_\odot \text{ keV}} \right)^{(0.57 \pm 0.03)} E(z)^{-2/5}, \quad (5)$$

also from Vikhlinin et al. (2009a), and iteratively determine Y_X and the total mass within r_{500} (see Section 3.5 below).

For each cluster, the center of the X-ray emission is determined using a centroid calculation. X-ray point sources were excluded in this process. The distance between the X-ray centroid and the SPT position is listed in Table 2. The SZ and X-ray positions given are both centroid measurements. However, due to the different weighting of their signals on the ICM density and temperature, the centroids are not expected to agree for a cluster which is not azimuthally symmetric. For *Chandra* data, point sources were identified using the CIAO tool *wavdetect* and removed from subsequent analysis. In the *XMM-Newton* data, point sources were detected with the SAS task *edetect chain*. Additionally, extended secondary maxima were identified and removed following the method prescribed in Vikhlinin et al. (2009a). Extended substructures were included in the estimation of the total cluster luminosity.

3.3. Spectral Analysis

Spectra and response files were generated from the *Chandra* data for the spectral extraction regions using *specextract*. We use two independent methods of background subtraction in this work and compare the results, and fit the spectra in the 0.5–7.0 keV band. Due to the limited spatial extent of most of the SPT candidates, it is possible to use in-field background

²⁶ This equation contains a typo in Vikhlinin et al. (2009a), Table 3, where the h -dependence was omitted, resulting in a different value of α (here $\alpha = 0.0225 h^{-1.5}$).

Table 3
X-ray Observables $T_{X,500}$, $M_{g,500}$, $Y_{X,500}$, and $L_{X,500}$ (0.5–2.0 keV)

Name	z	$T_{X,500}$ (keV)	$M_{g,500}$ ($10^{13} M_{\odot}$)	$Y_{X,500}$ ($10^{14} M_{\odot}$ keV)	$L_{X,500}$ (10^{44} erg s $^{-1}$)
J0000-5748 ^a	0.74	$8.6^{+3.8}_{-2.3}$	$4.7^{+0.5}_{-0.6}$	4.7 ± 1.8	5.7 ± 0.4
J0509-5342	0.4626	$7.0^{+1.4}_{-1.1}$	$5.6^{+0.2}_{-0.2}$	4.3 ± 0.8	3.2 ± 0.1
J0516-5430	0.2952	$9.8^{+1.7}_{-1.2}$	$17.0^{+0.4}_{-0.4}$	15.9 ± 2.4	4.7 ± 0.1
J0528-5300 ^a	0.7648	$5.2^{+3.5}_{-1.7}$	$2.9^{+0.4}_{-0.4}$	1.7 ± 0.9	1.9 ± 0.2
J0533-5005 ^a	0.8810	$4.0^{+1.9}_{-1.2}$	$2.1^{+0.5}_{-0.4}$	0.9 ± 0.4	1.2 ± 0.3
J0546-5345	1.0665	$7.5^{+1.7}_{-1.1}$	$7.3^{+0.4}_{-0.3}$	5.3 ± 1.0	6.4 ± 0.4
J0551-5709 ^b	0.4230	$4.1^{+0.9}_{-0.7}$	$5.1^{+0.3}_{-0.4}$	2.0 ± 0.4	1.9 ± 0.2
J0559-5249	0.6112	$7.7^{+1.1}_{-0.8}$	$8.3^{+0.3}_{-0.2}$	6.1 ± 0.8	3.3 ± 0.2
J2331-5051	0.5707	$5.9^{+1.3}_{-0.8}$	$5.7^{+0.2}_{-0.2}$	3.5 ± 0.6	4.4 ± 0.2
J2332-5358	0.32	$7.4^{+1.2}_{-0.7}$	$5.6^{+0.2}_{-0.2}$	4.4 ± 0.6	3.0 ± 0.1
J2337-5942	0.7814	$8.9^{+2.0}_{-1.4}$	$9.5^{+0.4}_{-0.6}$	8.5 ± 1.7	8.9 ± 0.5
J2341-5119	0.9983	$8.0^{+1.9}_{-1.6}$	$5.6^{+0.2}_{-0.2}$	4.7 ± 1.0	5.6 ± 0.3
J2342-5411 ^a	1.08	$5.0^{+0.9}_{-0.8}$	$2.6^{+0.3}_{-0.3}$	1.4 ± 0.3	2.9 ± 0.3
J2355-5056	0.35	$5.5^{+1.0}_{-0.8}$	$4.4^{+0.2}_{-0.1}$	2.6 ± 0.4	2.1 ± 0.1
J2359-5009 ^a	0.76	$6.4^{+2.3}_{-1.8}$	$2.8^{+0.3}_{-0.3}$	2.2 ± 0.7	1.6 ± 0.2

Notes.

^a Low signal-to-noise within the [0.15–1] r_{500} aperture. $T_{X,500}$ is estimated using the temperature within [0.15–0.5] r_{500} and scaled using Equation (8).

^b SPT-CL J0551-5709 is coincident with AS0552. The gas temperature is estimated through Equation (8).

subtraction. Background was extracted from regions near the source but outside of the r_{500} radius where the source flux is a small fraction of the background flux. Since the nominal pointing was chosen to be offset from the cluster position it is possible to extract the background at a detector coordinate where the mirror effective area is similar to that of the source extraction region and where the particle-induced background is similar. This limits complications related to undersubtracted X-ray background which can be a problem when using in-field background.

As a second background subtraction method we also use the latest blank field backgrounds collected by M. Markevitch,²⁷ re-project these on the sky to match our cluster data sets, and normalize the exposure times to match the count rates in the 9.5–12 keV band. The background spectra can then be extracted from the same detector region as the source. To correct for possible variation of the flux of the soft X-ray background between the source and blank field data, we fit a thermal model to a background-subtracted spectrum from a source-free region in the field. This model is scaled by the ratios of extraction areas and included as a fixed component in the cluster spectral fit. In all cases we find that the corrected spectral fit implies a temperature that is consistent with the uncorrected model. We compare the temperatures and flux estimates from the blank-sky and in-field techniques and find good agreement for all clusters. Since the blank-field background subtraction provides better S/N, we use this method throughout as this allows for temperature estimates within the r_{500} aperture for most objects.

For the *XMM-Newton* observations we use the spectral analysis as described in Andersson & Madejski (2004) and Andersson et al. (2009). For this work we limit the analysis to use in-field background since the *XMM-Newton* spectra have sufficiently high S/N, and the spatial extent of the sources is small.

Spectra for both *Chandra* and *XMM-Newton* data sets were extracted inside r_{500} , excluding the central emission within 0.15 r_{500} to avoid the effects of cool cores, known to cause additional scatter in X-ray scaling relations. We model the data using a MEKAL model for the thermal plasma with emission lines and a Wisconsin absorption (WABS) model. For our sample, the data are not deep enough to measure metal abundances reliably and we fix the abundance to 0.3 solar. The hydrogen equivalent absorbing column, n_{H} , was fixed at the weighted average from the Leiden–Argentine–Bonn survey (Kalberla et al. 2005). These are listed in Table 2. The best-fit temperatures are shown in Table 3.

3.4. X-Ray Imaging

The X-ray surface brightness is extracted in n concentric annuli defined by

$$r_i = \left(\frac{i}{n}\right)^c \times r_{\max} \quad i = 1, \dots, n, \quad (6)$$

where we have used $r_{\max} = 1.5r_{500}$, $c = 1.2$, and $n = 20$. The limiting radius r_{\max} is chosen to be large enough so that the cluster emission is negligible compared to the background and so that the integrated gas density is not overestimated due to projection effects. The values of c and n are chosen to balance high central resolution with achieving a similar number of X-ray counts per radial bin.

For every annular region the average exposure is calculated, taking into account bad pixels and chip gaps. Similarly, the average effective mirror area is calculated for each region taking into account the mirror vignetting. The radial model for the X-ray counts includes a component for the cluster X-ray surface brightness, a spatially flat unvignetted component for the particle induced, quiescent background plus an additional spatially flat, vignetted component for the X-ray background contribution.

The cluster surface brightness is taken to be proportional to the integrated emission measure, $\text{EM} = \int n_e n_p dV$, which is a

²⁷ <http://cxc.harvard.edu/contrib/maxim/acisbg>

good approximation in the 0.5–2 keV band for gas temperatures present in our sample. The inferred density distribution has been shown previously to have little dependence on the temperature when determined from the surface brightness in this energy band (Mohr et al. 1999; Forman et al. 2007). The radial gas density distribution is modeled using a modified β -model,

$$n_p n_e = n_0^2 \frac{(r/r_c)^{-\alpha}}{(1+r^2/r_c^2)^{3\beta-\alpha/2}} \frac{1}{(1+r^\gamma/r_s^\gamma)^{\epsilon/\gamma}}, \quad (7)$$

(Vikhlinin et al. 2006). The model accounts for the cuspy centers of clusters as well as the steepening of the profile seen at larger radii. We fix $\gamma = 3$ in the above expression (see Vikhlinin et al. 2006). For the *XMM-Newton* data, the projected model is convolved with a model of the *XMM* point-spread function (PSF), as described in Ghizzardi (2001), prior to fitting.

For both the *Chandra* and *XMM-Newton* data, the model is normalized by integrating Equation (7) over a cylindrical volume with a radius of r_{500} , truncated at $3r_{500}$ along the line of sight. This is compared to the spectral normalization of a MEKAL model with parameters derived in Section 3.3 within r_{500} . This way the model normalization, n_0 , can be calculated using the angular distance D_A determined from the redshift listed in Table 2. The gas mass $M_{g,500}$ is calculated by setting $n_e = Zn_p$ and $\rho_g = m_p n_e A/Z$, where $Z = 1.199$ and $A = 1.397$ are the average nuclear charge and mass, respectively, for a plasma with 0.3 solar abundances (implying a mean molecular weight per free electron $\mu_e = 1.165$) assuming abundances by Anders & Grevesse (1989). The gas density ρ_g is integrated over a sphere of radius r_{500} determined iteratively for M_g and Y_X estimates using $M_{500}-M_g$ and $M_{500}-Y_X$ relations, respectively.

The parameter space of the model is explored via Markov chain Monte Carlo iteration and the uncertainties on the parameters are estimated using the Markov chain posterior.

3.4.1. Cluster Images

X-ray images in the 0.5–2.0 keV band are generated using the filtered event files and binned into $4'' \times 4''$ pixels. These are shown in Figures 5–19 alongside optical images of the clusters from High et al. (2010). Images are smoothed with a $8''$ Gaussian filter. The images are shown with SZ S/N contours from V10 and the white crosses show the location of the brightest cluster galaxy (BCG). Solid contours are shown for positive SZ significance, $\xi > 0$, dashed contours are shown for $\xi \leq 0$. In all cases, the SPT detection is within $1'$ of the X-ray centroid and in a majority of cases (9 of 15) it is within $20''$. Additionally, Sydney University Molonglo Sky Survey (SUMSS; Mauch et al. 2003) radio sources are marked in the images with small circles ($15''$ radius). Extended X-ray structures are marked with larger circles ($30''$ radius) or arrows and are discussed for each individual cluster in the Appendix.

From visual inspection of the images, we note that there appears to be a large number (>5) of clusters with centrally peaked surface brightness profiles in the sample, many at high redshift ($z > 0.7$). A detailed study of the cool core fraction in this sample, and its relation to other work, is the subject of an upcoming study (K. E. Andersson et al., in preparation).

3.5. ICM Temperature, Gas Mass, Luminosity, and Y_X

The average spectral temperature of the ICM is measured within the $[0.15-1]r_{500}$ aperture as described in Section 3.3.

A new value of r_{500} is then estimated using this temperature with Equation (1) and a new spectrum is extracted using the new radius. The process is repeated until the value of T_X has converged. For five of the clusters, the number of source photons within $[0.15-1]r_{500}$ is less than 1000 and the S/N is less than 20. This leads to large uncertainties in the spectral fits and could potentially cause systematic biases in the temperature. For these objects, we instead use the estimate of T_X within $[0.15-0.5]r_{500}$, where the S/N is higher and extrapolate using the fitted relation between the two temperatures from Vikhlinin et al. (2009a):

$$T_{X,(0.15-1)r_{500}}/T_{X,(0.15-0.5)r_{500}} = 0.9075 + 0.0625 T_{X,(0.15-0.5)r_{500}}. \quad (8)$$

We also add a 10% uncertainty to these temperature estimates to account for the uncertainty in this relation. The clusters for which this procedure was performed are marked in Table 3. For SPT-CL J0551-5709, a cluster which is spatially coincident with the local cluster AS0552, we also perform this procedure, but with a different motivation. The surface brightness to the south and northwest of this cluster suggests that there is a significant amount of flux from cooler gas associated with the Abell cluster. This is also seen in the temperature estimates. T_X drops from 4.4 ± 0.7 keV to 3.3 ± 0.4 keV when comparing the inner and outer apertures. We include SPT-CL J0551-5709 in the scaling relation fits using the corrected temperature and mark it with a red square in the scaling relation plots. To check for any bias in the gas mass estimate, we also fit the gas density profile to the surface density, excluding the regions of enhanced flux. We find a good match to the gas mass estimate using the full profile and conclude that the foreground emission is captured by the background model.

Similarly, the gas mass within r_{500} , $M_{g,500}$, is estimated as described in Section 3.4 using an initial estimate of r_{500} from Equation (1) and the spectrally derived temperature, T_X . The estimate of r_{500} is then revised using the implied gas mass fraction and Equation (4), and the process is repeated until the gas mass converges.

In this work, we adopt redshift evolution of $f_{g,500}$, in the same way as it was applied in the work of Vikhlinin et al. (2009a). The redshift dependence of the gas-mass fraction is not well constrained observationally to high- z and independent measurements of the mass are needed to study this further. The $f_{g,500}-M$ relation is used here only to determine the radius r_{500} within which to estimate M_g and has no impact on the Y_X -based mass estimates. We do not quote any total masses based on the $f_{g,500}-M$ relation in this work.

SPT-CL J0516-5430 has an unusually extended morphology compared to other objects in the sample and the assumption of spherical symmetry is very approximate. The line-of-sight dimension for this cluster and the inferred gas mass are likely to be overestimated for this reason (see, e.g., Nagai et al. 2007). To keep the analysis analogous to Vikhlinin et al. (2009a), we do not attempt to correct for this here. SPT-CL J0516-5430 is marked with a blue triangle in the scaling relation plots.

When estimating Y_X , we use Equation (5) to determine r_{500} and re-calculate both T_X and M_g in a similar way. Cluster simulations show that Y_X exhibits less scatter with mass compared to M_g and T_X individually due to the typical anti-correlation of deviations from the mean of these two observables (Kravtsov et al. 2006). This makes the Y_X mass estimator less dependent on the dynamical state of clusters, as far as it can be estimated from simulations. The X-ray observables are listed in Table 3.

Table 4
Cluster Masses from M_{500-Y_X} and M_{500-T_X} Relations

Name	z	r_{500}^a (kpc)	M_{500,Y_X} ($10^{14} M_\odot$)	M_{500,T_X} ($10^{14} M_\odot$)	$M_{500,SZ,V10}^b$ ($10^{14} M_\odot$)
J0000-5748	0.74	950	5.32 ± 1.16	6.74 ± 3.99	$2.59 \pm 0.71 \pm 0.31$
J0509-5342	0.4626	1062	5.43 ± 0.60	6.71 ± 1.69	$3.70 \pm 0.81 \pm 0.48$
J0516-5430	0.2952	1463	11.84 ± 1.25	12.34 ± 2.57	$5.40 \pm 1.03 \pm 0.84$
J0528-5300	0.7648	775	2.97 ± 0.89	3.05 ± 2.65	$2.56 \pm 0.70 \pm 0.28$
J0533-5005	0.8810	656	2.06 ± 0.53	2.25 ± 1.29	$2.51 \pm 0.66 \pm 0.28$
J0546-5345	1.0665	840	5.33 ± 0.62	5.25 ± 1.37	$3.18 \pm 0.66 \pm 0.43$
J0551-5709	0.4230	948	3.56 ± 0.43	3.00 ± 0.80	$3.49 \pm 0.83 \pm 0.48$
J0559-5249	0.6112	1043	6.40 ± 0.54	7.07 ± 1.24	$4.59 \pm 0.88 \pm 0.61$
J2331-5051	0.5707	972	4.70 ± 0.51	4.91 ± 1.20	$4.17 \pm 0.84 \pm 0.57$
J2332-5358	0.32	1134	5.66 ± 0.48	6.69 ± 1.37	$4.34 \pm 0.90 \pm 0.64$
J2337-5942	0.7814	1046	7.43 ± 0.90	8.10 ± 2.14	$5.95 \pm 1.07 \pm 0.87$
J2341-5119	0.9983	847	5.06 ± 0.66	5.20 ± 1.82	$3.93 \pm 0.74 \pm 0.53$
J2342-5411	1.08	647	2.47 ± 0.32	2.39 ± 0.69	$2.56 \pm 0.61 \pm 0.34$
J2355-5056	0.35	1014	4.18 ± 0.43	4.26 ± 1.11	$3.46 \pm 0.85 \pm 0.48$
J2359-5009	0.76	816	3.45 ± 0.67	4.97 ± 2.21	$2.59 \pm 0.71 \pm 0.40$

Notes. Masses estimated from X-ray mass-proxy relations in Equations (1) and (5). SZ-derived masses from V10 are shown for comparison.

^a Estimated using the M_{500-Y_X} relation (Equation (5)).

^b Quoted masses from V10 include statistical and systematic uncertainties and have been scaled with our adopted h . The masses have been corrected for a bug in V10 when converting from $M_{200}(\rho_{\text{mean}})$ to $M_{500}(\rho_{\text{crit}})$.

For some of the clusters in the sample, the X-ray data are not deep enough to detect the X-ray emission with high significance out to r_{500} . For five of the clusters, the S/N in our radial bins (Equation (6)) drops below 3 at a radius of about $0.6 r_{500}$. These are the same five objects with low S/N spectra described above. The gas density profile is then constrained primarily by the central surface brightness profile and extrapolated out to r_{500} . This leads to systematic uncertainties that are difficult to account for as they depend on cluster morphology. In our sample we find a typical density slope $\rho_g \propto r^\alpha$ of $\alpha = -1.90 \pm 0.30$ at $0.6 r_{500}$, where we quote the mean and standard deviation. Varying the slope outside of this radius by ± 0.30 typically changes the mass outside $0.6 r_{500}$ by 8%. This is also an overestimate of the uncertainty since density profiles generally become steeper with increasing radius out to r_{500} . To be conservative, we add an uncertainty of 10% on the total gas mass for clusters with poor S/N outside $0.6 r_{500}$.

4. TOTAL MASS ESTIMATES

Using the mass proxies T_X and Y_X , we estimate the gravitational mass, M_{500} , for the clusters using Equations (1) and (5). The mass estimates are listed in Table 4. Clusters are identified as mergers based on their morphology. Clusters with secondary maxima, filamentary structure or significant isophotal centroid shifts are classified as unrelaxed (e.g., Mohr et al. 1993). As discussed in Kravtsov et al. (2006), the T_X -based masses should be multiplied by a factor 1.17 for clusters identified as mergers. Following Vikhlinin et al. (2009a), we correct our masses upward with this factor and add an uncertainty of 5% on the masses (Table 4). Our merger classification is listed in Table 2.

In Table 4, we also give the SZ-derived mass estimates from V10. In V10, the SPT cluster survey was used to constrain cosmological parameters while simultaneously fitting a cluster-detection-significance–mass relation. The significance–mass relation had priors imposed on its normalization, slope, and redshift evolution that were motivated by simulated thermal SZ maps of the sky. These maps were generated from large dark matter simulations (Shaw et al. 2009) that used a semi-analytic

gas model of Bode et al. (2007) which was calibrated such that the simulated clusters matched observed X-ray scaling relations for low-redshift ($z < 0.25$) clusters. The maximum-likelihood-significance–mass relation was then used to generate mass estimates for each cluster, including both statistical and systematic uncertainties. These systematic uncertainties were equivalent to a $\sim 15\%$ uncertainty on the mass estimate for each cluster.

Comparing the SZ- and X-ray-based mass estimates, we find that two clusters are 2σ inconsistent with a unit ratio and both have larger X-ray mass estimates; SPT-CL J0516-5430 and SPT-CL 0546-5345. V10 notes that clusters at $z < 0.3$ will have mass estimates biased low because the power-law scaling that is assumed for the significance–mass relation does not fully capture the effects of CMB-confusion on the SZ signal. This effect could possibly explain the relatively low SZ-inferred mass found for SPT-CL J0516-5430, which is the only cluster in this sample at $z < 0.3$ and was not used in the cosmological analysis in V10 for this reason. When considering the rest of the sample, we find that on average the SZ-derived masses are lower by a factor of 0.78 ± 0.06 , but note that including SPT-CL J0516-5430 does not significantly change the result.

This difference could have several explanations. For example, the semi-analytic gas model used to calibrate the simulations in V10 could have a redshift evolution that differs from self-similar evolution. There could also be differences in the gas profiles at large radii that cause systematic differences between the measured Y_X -based mass and the derived mass from the $M-\xi$ scaling in V10 that were not included in the simulations. For example, Shaw et al. (2010) found that variations in the level of feedback and non-thermal pressure support could significantly change cluster pressure profiles at $r > r_{500}$, where the SZ would be more sensitive. It should also be noted that the M_{500-Y_X} relation used here has been calibrated using X-ray hydrostatic mass estimates.

Numerical simulations have suggested that hydrostatic mass estimates could be biased low by $\sim 10\%$ due to additional non-thermal pressure support of the gas in clusters (e.g., Lau et al. 2009; Meneghetti et al. 2010). However, comparisons of hydrostatic and weak lensing mass estimates of low-redshift ($z < 0.3$) clusters show agreement at the $< 9\%$ level and suggest

no significant bias (e.g., Zhang et al. 2008; Vikhlinin et al. 2009a; Zhang et al. 2010).

Additionally, the $M_{500}-Y_X$ relation assumes self-similar redshift scaling. The details of redshift-dependent departures from this scaling are not well constrained observationally, although there is some observational evidence for $z \leq 0.6$ (Maughan 2007) and for a single cluster at $z = 1.05$ (Maughan et al. 2008) that self-similar evolution is reasonable. The results from simulations provide a 5% upper limit for any evolution of the amplitude of this relation between $z = 0$ and 0.6 (Kravtsov et al. 2006).

Regardless of the exact reasons, if the SZ mass estimates are biased low, there are consequences for the cosmological constraints in V10. The lower normalization of the SZ-significance–mass relation inferred from the X-ray measurements would indicate a larger value of σ_8 ; near the border of, but within, the 68% confidence region in V10 due to the restrictive priors on the parameters of the SZ-significance–mass relation. This result would be in broad agreement with the SZ power spectrum results from Lueker et al. (2010) and Shirokoff et al. (2011), by suggesting that the simulations are overpredicting the SZ signal for a halo of a given mass, therefore lowering the expected value of SZ amplitude for a given σ_8 . The cosmological implications of including the X-ray mass estimates with the V10 results will be the subject of a future paper.

5. SZ DATA ANALYSIS

5.1. Calculating Y_{SZ}

The SPT observations, data reduction, and mapmaking used in this work are identical to V10 and are outlined in Section 2.1. The analysis differs from V10 at the point where the SPT maps are spatially filtered to identify the cluster candidates. In our case, the cluster candidates have already been identified, and we instead want to calculate the SZ-inferred integrated Comptonization, Y_{SZ} , of each cluster. We calculate Y_{SZ} from the SPT 150 GHz maps by spatially filtering them using a filter motivated by the X-ray measurements of each cluster.

In V10, cluster candidates are identified by spatially filtering the SPT maps with a matched filter (Haehnelt & Tegmark 1996; Melin et al. 2006). This is done in the Fourier domain by multiplying the map by

$$\psi(k_x, k_y) = \frac{B(k_x, k_y)S(|\vec{k}|)}{B(k_x, k_y)^2 N_{\text{astro}}(|\vec{k}|) + N_{\text{noise}}(k_x, k_y)}, \quad (9)$$

where ψ is the matched filter, B is the response of the SPT instrument after timestamp processing to signals on the sky, S is the assumed source template, and the noise power has been broken into astrophysical (N_{astro}) and noise (N_{noise}) components. The noise covariance matrix N_{noise} includes contributions from atmospheric and instrumental noise, while N_{astro} includes power from primary and lensed CMB fluctuations, an unresolved SZ background, and unresolved point sources. In V10, the source template, S , was constructed from a projected spherical β -model.

In this work, we instead use an SZ source template motivated from X-ray measurements of each cluster. The SZ brightness is proportional to the line-of-sight integral of electron pressure or density times temperature. The profile is assumed to match the product of the best-fit gas density profile to the X-ray measurements of each cluster (Equation (7)), and the universal temperature profile of Vikhlinin et al. (2006; Equation (12)).

These profiles are multiplied together to give the radial pressure profile and projected onto the sky by doing a line-of-sight integral through the cluster. The radial pressure profile is truncated at $3 \times r_{500}$, where r_{500} is estimated using Equation (5) and given in Table 4. In constructing the spatial filter, we only need to know the spatial shape of the source, so the SZ model is normalized to unity.

For each of the 15 clusters, we construct a spatial filter using Equation (9) and a source model, as described above. The spatially filtered SPT maps are a measure of the normalization of each source model at the cluster location. Using the SPT maps alone to determine the cluster location would bias the Y_{SZ} measurements high because of the freedom to maximize the SPT significance by position. Therefore, we use the X-ray measured position as a prior on the cluster location. We define the uncertainty in the SPT normalization of the source model as the standard deviation of the spatially filtered map within a 90' band in declination around the cluster. The SPT maps are calibrated in units of K_{CMB} , the equivalent CMB temperature fluctuation required to produce the same power fluctuation. The SPT normalization is converted to Comptonization using the relation

$$\Delta T = y T_{\text{CMB}} \left(x \frac{e^x + 1}{e^x - 1} - 4 \right) [1 + \delta(x, T_e)], \quad (10)$$

where ΔT is the measured decrement in units of K_{CMB} , y is the Comptonization, T_{CMB} is the CMB blackbody temperature of 2.725 K, $x = h\nu/kT_{\text{CMB}}$, and $\delta(x, T_e)$ accounts for relativistic corrections to the SZ spectrum (Itoh et al. 1998; Nozawa et al. 2000). For the frequency-dependent terms in Equation (10), we calculate their SPT band averaged value, which would effectively correspond to an observing frequency, ν , of 152.9 GHz. The average SPT band is measured from Fourier Transform Spectroscopy measurements of a sample including more than 90% of the SPT 150 GHz detectors.

For the relativistic correction factor, $\delta(x, T_e)$, we assume an electron temperature of $T_{X,r500}/1.11$, where $T_{X,r500}$ is given in Table 3 and the factor of 1.11 is the average ratio of the X-ray-spectroscopic and mass-weighted temperature measured in Vikhlinin et al. (2006). The relativistic correction factor is only a weak function of temperature, over the range of cluster temperatures in this paper, 4.0–9.8 keV, $\delta(x, T_e)$ varies between -2.5×10^{-2} and -5.7×10^{-2} and we expect this assumption to negligibly affect our results.

The integrated Comptonization, $Y_{\text{SZ,cyl}}$, is calculated for each cluster by integrating its source model over solid angle, $Y_{\text{SZ,cyl}} \propto \int y(\theta)d\Omega$, normalized to the best-fit SPT Comptonization, y . To more easily compare to the X-ray measurements, we convert our measurements to units of M_{\odot} keV and define $Y_{\text{SZ,cyl}}$ as

$$Y_{\text{SZ,cyl}} = \left(\frac{\mu_e m_p m_e c^2}{\sigma_T} \right) D_A^2 \int y(\theta)d\Omega, \quad (11)$$

where D_A is the angular distance to the source, σ_T is the Thomson cross-section, m_e is the electron mass, m_p is the proton mass, c is the speed of light, and μ_e is the mean molecular weight per free electron. In Table 5, we give $Y_{\text{SZ,cyl}}$ integrated out to the angular radius corresponding to r_{500} as determined from the X-ray measurements and given in Table 4. The uncertainty in Y_{SZ} is calculated as the quadrature sum of the uncertainty in the SPT calibration, the measured SPT normalization of the source model, and an additional uncertainty in the assumed source model, which will be discussed in Section 5.3.

Table 5
Measured Cylindrical and Spherical Y_{SZ}

Name	z	$Y_{\text{SZ,cyl},500}$ ($10^{14} M_{\odot}$ keV)	$Y_{\text{SZ,sph},500}$ ($10^{14} M_{\odot}$ keV)
J0000-5748	0.74	3.0 ± 0.6	2.4 ± 0.5
J0509-5342	0.4626	3.9 ± 0.8	3.1 ± 0.6
J0516-5430	0.2952	15.3 ± 2.4	11.6 ± 1.8
J0528-5300	0.7648	2.6 ± 0.4	2.1 ± 0.4
J0533-5005	0.8810	1.8 ± 0.5	1.5 ± 0.4
J0546-5345	1.0665	4.6 ± 0.8	3.5 ± 0.6
J0551-5709	0.4230	3.7 ± 0.8	2.6 ± 0.6
J0559-5249	0.6112	7.6 ± 1.1	5.8 ± 0.9
J2331-5051	0.5707	5.0 ± 0.8	3.6 ± 0.6
J2332-5358	0.32	5.6 ± 1.0	4.9 ± 0.9
J2337-5942	0.7814	8.3 ± 1.0	7.1 ± 0.9
J2341-5119	0.9983	4.9 ± 0.7	4.1 ± 0.6
J2342-5411	1.08	2.3 ± 0.5	1.9 ± 0.4
J2355-5056	0.35	2.6 ± 0.6	2.2 ± 0.5
J2359-5009	0.76	2.1 ± 0.6	1.7 ± 0.5

5.2. Spherical Deprojection

Both the X-ray and SZ observations are measuring a projected signal that is proportional to the integrated gas properties in a line of sight through the cluster. This projection has different physical dependencies between X-ray and SZ observations that must be considered. To ease this comparison we deproject each measurement so that they correspond to a physical observable that is proportional to a spherical volume integral of each signal.

The Y_X estimates are deprojected as described in Section 3.4. For X-rays, the effect of the deprojection is smaller than for the SZ, because the X-ray flux is proportional to n_e^2 and only weakly dependent on temperature. This effect decreases the contribution to the X-ray signal from large radii where the density is lower. Also, Y_X will be proportional to an X-ray-spectroscopic-weighted temperature from gas between $0.15 r_{500}$ and r_{500} , while Y_{SZ} is related to the gas-mass-weighted temperature. We do not formally account for this difference in calculating either Y_X or Y_{SZ} . However, later in this section we will discuss this effect in interpreting their comparison.

We calculate $Y_{\text{SZ,sph}}$ by spherically deprojecting the $Y_{\text{SZ,cyl}}$ measurements in Table 5. The SZ signal is proportional to the line-of-sight integral of the electron density, n_e , times temperature, T_e . For each cluster, we assume the density profile derived from the X-ray imaging analysis and assume a temperature profile of a universal form,

$$T(r) = T_0 \frac{(x/0.045)^{1.9} + 0.45}{(x/0.045)^{1.9} + 1} \frac{1}{(1 + (x/0.6)^2)^{0.45}}, \quad (12)$$

where $x = r/r_{500}$ (see Vikhlinin et al. 2006). We then define $Y_{\text{SZ,sph}}$ as

$$Y_{\text{SZ,sph}} = \frac{Y_{\text{SZ,cyl}}}{C} = Y_{\text{SZ,cyl}} \frac{\int_{\text{sph}} T(r) n_e(r) dV}{\int_{\text{cyl}} T(r) n_e(r) dV}, \quad (13)$$

where C is the ratio of the integrals of pressure in a cylindrical and spherical volume through the cluster. For these integrals we use an integration radius of r_{500} and truncate the density and temperature radial models at $3 r_{500}$. We note that varying the truncation radius from between 3 and $5 r_{500}$ changes our measurement of Y_{SZ} in Table 5 by less than 1%. For the r_{500} aperture, the median and standard deviation of C across the

sample is 1.23 ± 0.08 . This is consistent with the value of 1.203 that is calculated assuming the universal pressure profile from Arnaud et al. (2010).

As noted earlier in this section, even after the above spherical deprojection, Y_X and $Y_{\text{SZ,sph}}$ are not directly comparable because of their different weighting of the electron temperature. Y_X is proportional to the X-ray-spectroscopic-weighted temperature, T_X , while $Y_{\text{SZ,sph}}$ is proportional to the mass-weighted temperature, T_{mg} . The size of this difference has been estimated by several authors from X-ray measurements. In Vikhlinin et al. (2006), they estimate $T_X/T_{mg} = 1.11$ for a sample of relaxed massive clusters with high angular resolution X-ray temperature measurements between 70 kpc and r_{500} . This would imply that $Y_{\text{SZ,sph}}/Y_X = 1/1.11 \approx 0.90$. In Arnaud et al. (2010), a similar analysis was performed for a sample that included both relaxed and unrelaxed clusters, and it was estimated that $Y_{\text{SZ,sph}}/Y_X = 0.924 \pm 0.004$. For the measured density profiles and assumed temperature profiles for our sample, we would expect an average ratio of $Y_{\text{SZ,sph}}/Y_X = 0.91 \pm 0.01$. To compute this expected ratio we have used the “spectroscopic-like” temperature (e.g., Mazzotta et al. 2004), given the density and temperature profiles used here.

In Section 6.2, we compare the above ratios, predicted purely from X-ray observations, to the ratio including the $Y_{\text{SZ,sph}}$ calculated from the SZ data as described in Section 5.1 and deprojected as described in this section.

5.3. Model Uncertainty

The integrated Comptonization, Y_{SZ} , inferred from the SZ data depends on the assumed spatial model through the construction of the spatial filter, and the volume integral through the deprojection of the SZ data. For a typical cluster, the X-ray data constrain the cluster density profile with high S/N out to $\sim r_{500}/2$ with no information on the temperature profile. Since a significant amount of the SZ signal is coming from larger radii than this, we would like to estimate how much uncertainty our assumed profile is adding to the Y_{SZ} estimates. To help do this, we calculate the Y_{SZ} of each cluster assuming the universal pressure profile of Arnaud et al. (2010), variations of the temperature profile in Equation (12), and an isothermal model.

Arnaud et al. (2010) measure a universal pressure profile from X-ray measurements for a representative set of local massive clusters. These measurements were deep enough to constrain the cluster density and temperature profiles out to r_{500} in each cluster. They find that their sample is well fit by a universal pressure profile that is defined only by M_{500} . For each cluster in our sample, we re-calculate $Y_{\text{SZ,sph}}$ assuming the universal pressure profile from Arnaud et al. (2010) and the X-ray-measured values for r_{500} and M_{500} given in Tables 5 and 4, respectively. Comparing these $Y_{\text{SZ,sph}}$ estimates to the values given in Table 5, we find that this ratio has a mean and standard deviation of 1.01 ± 0.15 averaged over the sample. There is one significant ($>20\%$) outlier, SPT-CL J0516-5430, whose $Y_{\text{SZ,sph}}$ deviates by a factor of 0.59. This cluster is a major merger, and the observed cluster profile is noticeably poorly fit by the Arnaud et al. (2010) pressure profile, which does not capture the disturbed distribution of the central gas in this cluster. Leaving this cluster out of our comparison, the average ratio becomes 1.03 ± 0.10 . Therefore, we see no detectable bias when assuming the Arnaud et al. (2010) pressure profile, but these results suggest that there could be an additional $\sim 10\%$ uncertainty in our $Y_{\text{SZ,sph}}$ measurements from our assumed pressure profile.

As an additional test, we vary the outer slope of the Vikhlinin et al. (2006) temperature profile in Equation (12), letting the exponent on the term in the right-hand side of the denominator vary between 0.16 and 0.80, from its starting value of 0.45. This range of values matches the full range of effective slopes of the temperature profile at r_{500} as measured in the sample of Vikhlinin et al. (2006). Calculating new $Y_{\text{SZ},\text{sph}}$ estimates assuming these new temperature profiles, we find that they change the $Y_{\text{SZ},\text{sph}}$ values given in Table 5 on average by a factor of 1.09 ± 0.06 and 0.91 ± 0.05 for the exponent values of 0.16 and 0.80, respectively. While we consider such a significant systematic shift in the temperature profile unlikely across the whole sample, this level of variation in temperature profiles could contribute added statistical uncertainty in the $Y_{\text{SZ},\text{sph}}$ estimates.

As a limiting case, we also recalculate $Y_{\text{SZ},\text{sph}}$ assuming that the cluster is isothermal and with a density profile corresponding to the best-fit profile to the X-ray measurements. Comparing $Y_{\text{SZ},\text{sph}}$ for the isothermal profile to the values given in Table 5, we find that this ratio has a mean and standard deviation of 1.12 ± 0.08 averaged over the sample. This is certainly an extreme case because of the abundance of evidence for the temperature profile in clusters decreasing significantly by r_{500} (e.g., Vikhlinin et al. 2006; Arnaud et al. 2010). Recent *Suzaku*-observations of nearby clusters at large radii also indicate a drop of gas temperature by a factor ~ 3 at r_{200} (e.g., Fujita et al. 2008; George et al. 2009; Bautz et al. 2009; Reiprich et al. 2009; Hoshino et al. 2010). We also note that the temperature profile with an exponent of 0.80 assumed in the previous paragraph would have a gas temperature that dropped by a factor of ~ 5 at r_{200} , so even this would seem like an extreme case.

Overall, we are encouraged that the variation in $Y_{\text{SZ},\text{sph}}$ is found to be $\sim 10\%$ when assuming a broad range of different temperature and pressure profiles found in the works of Vikhlinin et al. (2006) and Arnaud et al. (2010). Therefore, we conservatively assume an additional 10% statistical uncertainty in our $Y_{\text{SZ},\text{sph}}$ estimates from any assumed model uncertainty, which we have added in quadrature to the uncertainties given in Table 5.

5.4. Point-source Contamination

Astrophysical point sources in the direction of the cluster can potentially fill in the SZ cluster decrement and bias the integrated Comptonization low. There are generally two populations of sources that can contaminate the SZ signal: dusty or radio bright sources. In V10, the potential contamination from both was discussed, and neither is expected to significantly bias the SZ measurements at 150 GHz averaged over the sample. We review some of those conclusions here.

In the Appendix, we discuss radio detections at 843 MHz by the SUMSS toward the clusters in this work. The majority of radio sources in clusters have been found to have steep spectra with $\alpha < -0.5$ (where $S \propto \nu^\alpha$) (e.g., Coble et al. 2007; Lin et al. 2009). For example, Coble et al. (2007) find a median spectral index of -0.72 between 1.4 and 28.5 GHz for radio sources toward a sample of massive clusters ranging from $0.14 < z < 1.0$. In V10, they noted that a typical cluster would suffer a decrease of $\Delta\xi = 1$ for a 2 mJy (5 mJy) source at 150 GHz located at $0.5'$ ($1'$) from the cluster center. Assuming a spectral index of -0.72 , a 2 mJy (5 mJy) source at 150 GHz would be ~ 83 (210) mJy at the SUMSS observing frequency of 843 MHz. As detailed in the Appendix, no source has been detected above either threshold within $1'$

of any cluster in this work. However, for any individual cluster radio source, extrapolating its flux from radio frequencies to the SPT observing frequency of 152.9 GHz is difficult because of the broad range and frequency dependence of the spectral indices that is typical for these sources (e.g., Coble et al. 2007; Lin et al. 2009). In practice, extrapolating the flux of any SUMSS detected source to the SPT observing frequency will have factors of a few uncertainty without further observations spanning an intermediate range of frequencies. With this caveat in mind, there appears to be no source strong enough to significantly bias the SZ flux estimate for any cluster in this work.

Including every source detected within $0.5'$ of each cluster center in our sample, the cumulative SUMSS flux is 224.5 mJy. If we assume a spectral index of -0.72 , this would imply an average flux of ~ 0.35 mJy per cluster at 152.9 GHz. This would correspond to an average decrease in the SZ flux of $\sim 2\%$, assuming that these sources represent an overdensity to the background population.

The average radio source contamination in SZ surveys has been recently estimated in simulations of the microwave sky by Sehgal et al. (2010). These simulations were motivated by observations by Lin et al. (2009) measuring the radio source population characteristics in low-redshift ($z < 0.25$) X-ray-detected clusters. For the mass limit of this work, $M_{500} \approx 3 \times 10^{14} h^{-1} M_\odot$, these studies predict that in $\lesssim 1\%$ of clusters there would be radio source contamination large enough to affect the SZ flux measurement at the $> 20\%$ level, with this result largely independent of redshift. V10 estimate a similar rate of contamination using a radio source count model (de Zotti et al. 2005) and the measured overabundance of radio sources near clusters (Coble et al. 2007). Overall, the combination of the above results leads us to not expect any significant radio source contamination.

Emission from submillimeter bright galaxies can also contaminate the SZ signal. These sources are typically dusty star-forming galaxies that are very luminous but highly obscured, such that their luminosity is peaked at infrared (IR) wavelengths. The number counts and fluxes of these sources have been characterized between 0.5 and 2.0 mm wavelength by several experiments (e.g., Coppin et al. 2006; Devlin et al. 2009; Vieira et al. 2010; Austermann et al. 2010), and these measurements reasonably match simple analytic models describing their source population distribution (Lima et al. 2010b). These sources can largely be approximated as a random background that contributes additional signal in the SPT maps, and we have explicitly accounted for them in our matched filter in Equation (9). However, this implementation did not account for any emission that could be correlated with clusters, or additional noise from the background objects being gravitationally lensed by the cluster. The former was argued to be insignificant in V10 because the IR overdensity toward clusters is expected to be $\ll 1$ mJy at 150 GHz even out to highest redshift clusters in our sample, and observational measurements of the $100 \mu\text{m}$ flux toward local clusters ($z \sim 0.2$) are too low to significantly bias the SZ flux measurements even allowing for a strong redshift evolution of these sources. The latter has been characterized by Lima et al. (2010a) to increase the flux noise toward clusters by $\sim 60\%$, which is at a level such that it would be $\lesssim 3\%$ of the SZ flux for the mass range of clusters in our sample. We note that because lensing is a surface brightness conserving process, this latter effect would not bias our results when averaged over a large sample of clusters.

Table 6
X-ray and SZ Scaling Relations $\log(Y) = A + B \log(X/X_{\text{pivot}}) + C \log(E(z))$

Relation	A	B	C	σ_y	X_{pivot}
L_X-T_X	44.16 ± 0.09	1.92 ± 0.60	1	0.11 ± 0.06	5 keV
$L_{\text{bol}}-T_X$	44.64 ± 0.14	2.31 ± 0.85	1	0.17 ± 0.08	5 keV
$L_X-M_{Y,500}$	44.28 ± 0.04	1.18 ± 0.21	1.85	0.11 ± 0.04	$5 \times 10^{14} M_{\odot}$
M_g-T_X	13.70 ± 0.10	1.79 ± 0.51	-1	0.08 ± 0.05	5 keV
$Y_{\text{SZ,sph}}-Y_X$	14.40 ± 0.08	0.96 ± 0.18	0	0.09 ± 0.04	$3 \times 10^{14} M_{\odot} \text{ keV}$
$Y_{\text{SZ,sph}}-Y_X$	14.39 ± 0.04	1	0	0.09 ± 0.04	$3 \times 10^{14} M_{\odot} \text{ keV}$
$Y_{\text{SZ,sph}}-Y_X$	14.44 ± 0.08	1	-0.36 ± 0.58	0.09 ± 0.04	$3 \times 10^{14} M_{\odot} \text{ keV}$
$Y_{\text{SZ,cyl}}-Y_X$	14.50 ± 0.05	0.90 ± 0.17	0	0.07 ± 0.05	$3 \times 10^{14} M_{\odot} \text{ keV}$
$Y_{\text{SZ,cyl}}-Y_X$	14.49 ± 0.04	1	0	0.09 ± 0.04	$3 \times 10^{14} M_{\odot} \text{ keV}$
$Y_{\text{SZ,cyl}}-Y_X$	14.54 ± 0.09	1	-0.35 ± 0.56	0.09 ± 0.04	$3 \times 10^{14} M_{\odot} \text{ keV}$
$Y_{\text{SZ,sph}}-M_{Y,500}$	14.06 ± 0.10	1.67 ± 0.29	2/3	0.09 ± 0.05	$3 \times 10^{14} M_{\odot}$
$Y_{\text{SZ,sph}}-M_{Y,500}$	14.03 ± 0.04	1.79	2/3	0.09 ± 0.04	$3 \times 10^{14} M_{\odot}$

Notes. Self-similar $E(z)$ -scaling has been assumed here except for the $L_X-M_{Y,500}$ relation, where the best-fit evolution from (Vikhlinin et al. 2009a) is adopted. σ_y represents the intrinsic scatter in $\log Y$.

One noteworthy exception where point-source contamination is evident is the cluster SPT-CL J2332-5358. This cluster was the only candidate in V10 that was also coincident with a point source detected in the SPT 220 GHz maps at $>5\sigma$. Similar 220 GHz detected point sources have a source flux, S , that scales with frequency as $S \propto \nu^\alpha$ with $\alpha = 3.3 \pm 0.7$ between 150 and 220 GHz (Vieira et al. 2010). Extrapolating its measured 220 GHz source flux would predict a flux of 11.0 ± 2.7 mJy at 150 GHz. To the 150 GHz SPT maps, we subtract a point source of this brightness, after convolving it with the 150 GHz SPT transfer function. We then repeat the same cluster extraction method as in V10 to calculate a new cluster position and SPT significance, ξ , which is given in Table 2. This point source corrected 150 GHz map is used when calculating the Y_{SZ} given in Table 5, and the added uncertainty in Y_{SZ} from the uncertain point-source spectral index is added in quadrature with the other uncertainties outlined in Section 5.1.

6. SCALING RELATIONS

Here we discuss the X-ray and SZ scaling relations for the sample. We consider the integrated SZ flux Y_{SZ} for both cylindrical and spherical volumes of integration. The integrated cylindrical estimate is deprojected to a spherical estimate as described in Section 5.2.

To measure the slope and normalization of the scaling relations, we perform linear regression in the presence of intrinsic scatter. We use the Bayesian method of Kelly (2007) and maximize the probability of a linear model in log-log space, accounting for measurement uncertainties in both axes. For the Y_{SZ} -scaling relations below we fit the relations with another method, accounting for the ξ selection. We investigate this fitting method using simulated cluster samples as detailed in Section 6.2. We have assumed self-similar $E(z)$ -scaling for these scaling relations unless otherwise stated. The best-fit parameters for these relations are listed in Table 6.

6.1. M_g-T_X , L_X-T_X , and L_X-M_{500}

The scaling between the ICM gas mass (M_g) and the spectroscopic temperature (T_X) is an important test of the properties of this SZ-selected sample. We want to know if the SZ selection biases differ from those of X-ray-selected samples. The M_g-T_X relation can also be used to infer the gas mass fraction in clusters (e.g., Vikhlinin et al. 2009a). Any deviation from self-similar

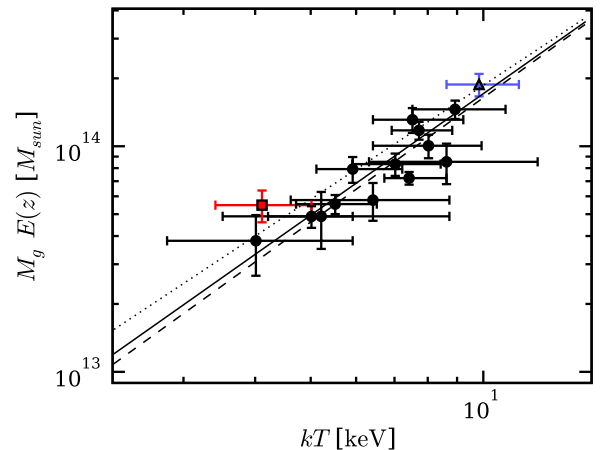


Figure 1. M_g-T_X relation with self-similar $E(z)$ -scaling. The data from the SPT sample are shown as circles with error bars and the solid line shows the best-fit scaling relation. For comparison, we also show the best-fit relations using the low- z (dashed line) and high- z (dotted line) samples from Vikhlinin et al. (2009a). These data were fitted using the same method described here. SPT-CL J0551-5709 is shown as a red square and SPT-CL J0516-5430 is shown with a blue triangle.

evolution in this relation could indicate an evolving gas mass fraction. Following Vikhlinin et al. (2009a), the values of M_g used for this relation were derived in a slightly different way compared to the description in Section 3.4. Instead of using M_g itself for the iterative determination of the extraction radius r_{500} , we use the measured temperature and Equation (1). This is done to minimize the correlation of the observables in the scaling relation and to avoid assumptions of possible evolution in Equation (4) in the determination of M_g .

We fit the relation

$$E(z)M_g = 10^A \left(\frac{T_X}{5 \text{ keV}} \right)^B M_{\odot} \quad (14)$$

to the data as described above, accounting for intrinsic scatter. Figure 1 shows the M_g-T_X relation with the best-fit power law (solid line). Here we have assumed self-similar evolution and search for deviations from this by comparing the fit parameters from cluster samples at different redshifts.

To compare our results with previous studies using X-ray-selected samples, we use the gas mass and temperature data for the low- z (median $z \approx 0.05$) and high- z (median $z \approx 0.48$)

as measured by Vikhlinin et al. (2009a), derived using the same method. We choose these samples since the data analysis is analogous to ours and use only clusters above 4 keV to probe a similar mass range as that of the SPT sample. We fit the scaling relation to these samples using the same method. For our SPT-selected sample (median $z = 0.74$), we find $A = 13.70 \pm 0.10$ and $B = 1.79 \pm 0.51$ (see Table 6). When fitting the low- z sample, we find $A = 13.68 \pm 0.01$ and $B = 1.77 \pm 0.08$, in good agreement with the SPT sample. For the high- z sample from Vikhlinin et al. (2009a), the best-fit parameters are $A = 13.75 \pm 0.02$ and $B = 1.53 \pm 0.27$, also consistent with the SPT result. The offset between the low- z and high- z samples of Vikhlinin et al. (2009a) indicates deviations from self-similarity. The slope of the low- z sample is significantly steeper than the expected self-similar slope of $B = 1.5$. A positive trend of the gas mass fraction with mass has been observed previously (e.g., Mohr et al. 1999; Vikhlinin et al. 2006) and is likely what is causing the steeper than self-similar slope of the relation. However, both the SPT sample and the high- z sample are consistent with the self-similar slope as well as that of the low- z sample.

Numerical simulations (e.g., Kravtsov et al. 2005) also show an increasing gas mass fraction with redshift, presumably due to a different distribution of cluster progenitors at high redshift. Clusters formed at high redshift have progenitor galaxies with a different mass function compared to low-redshift systems. Additionally, star formation is likely more efficient in high mass galaxies which would cause a redshift dependence of the gas fraction since there will be different ratios of gas converted into stars (see the discussion in Vikhlinin et al. 2009a). The SPT result is not sensitive enough to distinguish between this scenario and that of a constant gas mass fraction. The normalization agrees well with that of both the low- z and high- z samples of Vikhlinin et al. (2009a). Comparing the high- and low- z samples of Vikhlinin et al. (2009a) directly, we note that they indicate a 3σ significant deviation from self-similar evolution of the M_g-T_X relation between $z \approx 0.05$ and $z \approx 0.48$ at 5 keV.

We cannot rule out that this behavior is partly related to deviations from self-similarity in the $M-T_X$ relation at high redshift.

We also investigate the luminosity–temperature relation (e.g., Edge & Stewart 1991; Markevitch 1998) for the sample where we compare the luminosity in the 0.5–2.0 keV band within r_{500} , including the core, L_X , to the temperature estimate within r_{500} , T_X , with the core excised. We fit the relation

$$E(z)^{-1} L_X = 10^A \left(\frac{T_X}{5 \text{ keV}} \right)^B \text{ erg s}^{-1} \quad (15)$$

and find a shallow slope, $B = 1.92 \pm 0.60$ (see Table 6), consistent with previous work (e.g., Markevitch 1998), although other work finds a slope close to 3 (e.g., Mantz et al. 2010). For completeness, we also estimate the bolometric luminosity by extrapolating the spectrum for all frequencies using the core-excised temperature. This introduces additional uncertainties on the luminosity due to the uncertainty in the temperature estimate. For the $L_{\text{bol}}-T_X$ relation, we find a steeper slope of $B = 2.31 \pm 0.85$, consistent with previous work (e.g., Markevitch 1998; Pratt et al. 2009). The best-fit relation is shown in Figure 2 (left).

We investigate the luminosity–mass relation (e.g., Reiprich & Böhringer 2002) and adopt the best-fit $E(z)$ -scaling found by

Table 7
X-ray Scaling Relations $\log(Y) = A + B \log(X/X_{\text{pivot}}) + C \log(E(z))$,
BCES Fit

Relation	A	B	C	X_{pivot}
L_X-T_X	44.05 ± 0.08	2.90 ± 0.77	1	5 keV
$L_{\text{bol}}-T_X$	44.48 ± 0.12	3.46 ± 0.69	1	5 keV
$L_X-M_{Y,500}$	44.28 ± 0.03	1.46 ± 0.24	1.85	$5 \times 10^{14} M_\odot$
M_g-T_X	13.68 ± 0.06	1.97 ± 0.46	-1	5 keV

Notes. Self-similar $E(z)$ -scaling has been assumed here except for the $L_X-M_{Y,500}$ relation, where the best-fit evolution from (Vikhlinin et al. 2009a) is adopted.

Vikhlinin et al. (2009a) to fit for the relation

$$E(z)^{-1.85} L_X = 10^A \left(\frac{M_{500,Y_X}}{5 \times 10^{14} M_\odot} \right)^B \text{ erg s}^{-1}. \quad (16)$$

The best-fit relation is shown in Figure 2 (solid line) compared to the best fit in Vikhlinin et al. (2009a; dashed line). We find a slope of $B = 1.18 \pm 0.21$, shallow compared to the $B = 1.61 \pm 0.14$ found by Vikhlinin et al. (2009a), while the normalization agrees very well near the median mass of the sample at $5 \times 10^{14} M_\odot$. From the relation in Vikhlinin et al. (2009a), we expect a normalization of $A = 44.25$ at $5 \times 10^{14} M_\odot$, which is in good agreement with our measured value of $A = 44.28 \pm 0.04$. The evolution exponent in the relation of Vikhlinin et al. (2009a) also has an uncertainty -1.85 ± 0.42 , corresponding to a $\sim 20\%$ uncertainty on the normalization at $z = 0.7$. The slope of the fit is mostly driven by SPT-CL 0516-5430 (blue triangle) which has a high derived mass for its measured luminosity, possibly caused by the observed merging activity in the cluster. Excluding this object from the fit changes the slope to $B = 1.45 \pm 0.29$, consistent with Vikhlinin et al. (2009a).

For completeness, we also perform fits of the X-ray scaling relations using the bivariate correlated errors and intrinsic scatter (BCES) linear regression estimator (Akritas & Bershady 1996), the results of which are listed in Table 7. In all cases, we find a better agreement with expectations from previous studies, as listed earlier in this section, compared to the fit using the Bayesian method of Kelly (2007). We note that commonly used linear regression estimators have been shown to give biased results, particularly in cases where the sample size is small and/or the measurement errors are large (see Kelly 2007 for a discussion).

In summary, we find a good agreement between the X-ray observables measured for this SZ-selected sample when comparing our results to X-ray-selected samples where similar analysis methods were used.

6.2. Y_{SZ} Scaling Relations

6.2.1. Fitting Method

The selection of clusters above a fixed S/N threshold can bias the SZ–X-ray-scaling relations. The SZ flux, Y_{SZ} , is correlated with the SZ S/N on which the sample is selected and ignoring this effect will lead to bias in the Y_{SZ} -scaling relation parameters. The steepness of the cluster mass function makes this bias more of a problem since the number of clusters in a given mass bin grows exponentially toward lower masses. This causes more clusters to be near the selection threshold where the effect is most prominent. The measurement uncertainty in Y_{SZ} and the intrinsic scatter in the scaling relation cause clusters with low mass (or

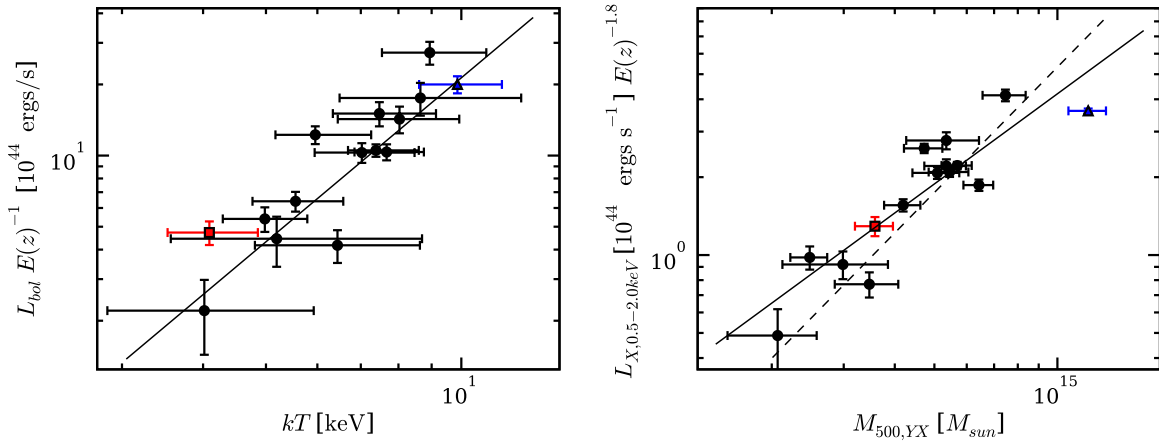


Figure 2. $L_{\text{bol}}-T_X$ (left) and L_X-M_{500,Y_X} (right) relations for the sample. For the $L_{\text{bol}}-T_X$ relation, we have applied self-similar $E(z)$ -scaling. For the L_X-M_{500,Y_X} relation, we have applied $E(z)^{1.85}$ -scaling to enable comparison with Vikhlinin et al. (2009a) shown with a dashed line. Solid lines represent the best-fit relation. SPT-CL J0551-5709 is shown as a red square and SPT-CL J0516-5430 is shown with a blue triangle.

Y_X) to scatter over the selection threshold. This is visible as a tail toward low mass (or Y_X) near the Y_{SZ} -selection threshold in the scaling relation plots. If ignored, this bias will lead to a biased slope and a higher normalization near the threshold in the fitted scaling relation parameters. Below we describe our method to account for the SZ selection in our scaling relation fits.

We estimate how the selection cut in ξ translates to a selection in $Y_{\text{SZ},\text{sph}}$ using simulated SPT observations. We repeat the procedure used in V10 to estimate the SZ selection function and SZ-significance–mass relation, where observations of simulated SZ maps are added to the dominant sources of astrophysical confusion and instrumental noise, mock observed, and processed through the SPT analysis pipeline. In contrast from V10, we keep track of the predicted value of $Y_{\text{SZ},\text{sph}}$ for each cluster, which is estimated using the $Y_{\text{sph}}-M_{500}$ scaling relation from Arnaud et al. (2010) and the simulated cluster’s mass, M_{500} . Also, we measure ξ for each simulated cluster in the same way as we do for the SPT observations, where we record the maximum significance S/N over different spatial filters and in a single realization of the astrophysical confusion and noise.

With these results we find a best-fit relation

$$\xi = 5.90 \left(\frac{Y_{\text{SZ}}}{2 \times 10^{14} M_{\odot} \text{ keV}} \right)^{0.64} E(z)^{0.16} \quad (17)$$

with intrinsic scatter in $\log Y_{\text{SZ}}$ of 0.10. Comparing this result with the measured ξ and Y_{SZ} for our sample, we find that the simulation-based relation is offset slightly high in ξ . When fitting the normalization of the above relation with the observed data, we find a best-fit value of 5.56 ± 0.31 , about 6% lower than the simulations suggest. The reason for this offset may be related to systematic uncertainties in the simulation of SPT observations. We adopt this best-fit normalization from the observed data and use the above relation to construct a selection function in $\log Y_{\text{SZ}}$. We estimate the selection probability as an error function in $\log Y_{\text{SZ}}$ at this threshold with the width set by the intrinsic scatter in this relation. To account for the uncertainty in the simulations we use a 10% Gaussian uncertainty on the normalization and a 20% Gaussian uncertainty on the intrinsic scatter, which we marginalize over for our results.

The Y_{SZ} -scaling relation fit is performed as follows. First, we calculate the probability of measuring a certain Y_{SZ} for a given M or Y_X and a given scaling relation with lognormal scatter. This is then convolved with the measurement uncertainty in Y_{SZ} . The

Y_{SZ} -selection cut is applied by multiplying the probability of measuring Y_{SZ} with an error function in $\log Y_{\text{SZ}}$ as described above. The likelihood is then calculated as the product of probabilities for all clusters and is maximized to obtain the scaling relation parameters.

We note that the scatter in Y_{SZ} and Y_X with the true cluster mass will be partially correlated. The scatter is expected to be at a level smaller than both the statistical uncertainty of our measurements and the intrinsic scatter in the ξ -mass relation. Because we have limited statistical constraining power with 15 clusters, we fit for the intrinsic scatter in the $Y_{\text{SZ}}-M_{500,Y_X}$ and $Y_{\text{SZ}}-Y_X$ relations assuming zero correlated scatter between Y_{SZ} and Y_X .

To test our fitting method for potential biases, we run it on mock samples drawn from a fiducial mass function. We perform this test both in the limit of a sample with 1000 clusters and for many samples of 15 clusters. To estimate a Y_{SZ} for the mock samples, we assume a $Y_{\text{SZ}}-M$ relation with lognormal scatter and convolve this with a linear measurement scatter of $0.4 \times 10^{14} M_{\odot}$. We assume that we know the relation between ξ and Y_{SZ} and its scatter to reproduce the sample selection function. In the limit of a large sample of clusters, we find no measurable bias in either the fitted slope or normalization. For 1000 generated mock samples of 15 clusters, we find that the scatter in normalization and slope between the samples and the average measurement error on the parameters over the samples are consistent. The normalization is reproduced to within 0.1% of the input value while we find that the slope is biased low by 2.0%. The average measurement error on the slope from the 15 cluster samples is 13.5% so this bias is of little significance.

6.2.2. $Y_{\text{SZ}}-Y_X$ Relation

The relationship between Y_{SZ} and Y_X is determined by details of the gas and temperature distribution in the cluster. It is effectively measuring a relationship between the mass-weighted and X-ray-spectroscopic-weighted temperature. In Arnaud et al. (2010), X-ray measurements of both relaxed and unrelaxed clusters were used to approximate a $Y_{\text{SZ}}-Y_X$ relation, for a spherical integration to r_{500} . Their work found a relationship with a normalization of 0.924 ± 0.004 , implying a lower mass-weighted temperature. This result is consistent with previous X-ray measurements (e.g., Vikhlinin et al. 2006), and our expectation of 0.91 ± 0.01 for the measured gas density

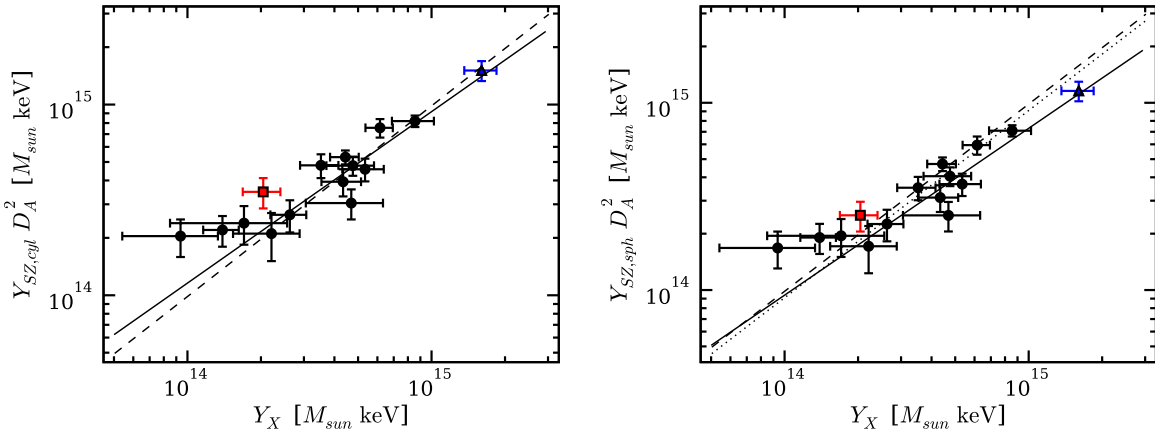


Figure 3. $Y_{\text{SZ}} - Y_X$ relation for the sample. The plots show uncorrected $Y_{\text{SZ},\text{cyl}}$ estimates (left) and the deprojected $Y_{\text{SZ},\text{sph}}$ estimates assuming a universal temperature profile (right). The solid line shows the best-fit relation. The dashed lines represent equality and the dotted line is the best-fit relation from Arnaud et al. (2010). SPT-CL J0551-5709 is shown as a red square and SPT-CL J0516-5430 is shown with a blue triangle.

profiles and the assumed temperature profile in this work. Hydrodynamical simulations predict a similar ratio, but also find that X-ray measurements could overestimate the integrated pressure at some level (e.g., Nagai et al. 2007). This would imply that the X-ray predictions of the normalization of the $Y_{\text{SZ}} - Y_X$ relation could be biased high; for example, the results of Nagai et al. (2007) suggest a bias at the few percent level.

Recently, there has been some evidence that the SZ signal from clusters could be lower than this expectation from comparison of *WMAP* SZ observations of X-ray-selected clusters (Komatsu et al. 2011), however similar analyses have led to different conclusions (Melin et al. 2011). By fitting a normalization of the $Y_{\text{SZ}} - Y_X$ relation to the clusters in this work, we can test for a similar offset, which could be indicative of differences in the real gas profiles from those we have assumed or some other systematic bias in either the SZ or X-ray measurement.

Using the method described in Section 6.2.1, we fit a scaling relation between Y_{SZ} and Y_X of the form

$$Y_{\text{SZ}} = 10^A \left(\frac{Y_X}{3 \times 10^{14} M_{\odot} \text{ keV}} \right)^B M_{\odot} \text{ keV}. \quad (18)$$

In Figure 3, we show the $Y_{\text{SZ}} - Y_X$ relation for both cylindrical (left) and spherical (right) Y_{SZ} , denoted by $Y_{\text{SZ},\text{cyl}}$ and $Y_{\text{SZ},\text{sph}}$, respectively. In Table 6, we give fits to Equation (18) given several different assumptions, which are described and discussed further below.

For both cylindrical and spherical Y_{SZ} , we find a slope consistent with unity and low scatter. It is possible that the scatter in the relation is suppressed since the Y_{SZ} estimates are derived using a density profile based on the X-ray data, although normalized independently. Based on the comparison of Y_{SZ} estimates using different pressure profiles (Section 5.3), we conclude that the possible additional scatter that could arise from using a different profile independent of the X-ray data is less than 10%. The dashed line in the plots is the $Y_{\text{SZ}} = Y_X$ relation and the dotted line (right) shows the expected $Y_{\text{SZ},\text{sph}}/Y_X$ ratio of 0.924 found in the work of Arnaud et al. (2010). We also fit the scaling relations with the slope fixed to 1 (see Table 6).

The normalization of our $Y_{\text{SZ},\text{sph}} - Y_X$ fit implies an average ratio of 0.82 ± 0.07 , offset by 1.5σ from the prediction of Arnaud et al. (2010). The marginally lower normalization found in this relation when compared to the X-ray prediction is expected at some level from hydrodynamical simulations which

predict that Y_{SZ} could be biased high from clumping (see the discussion in Nagai & Lau 2011) when estimated using X-ray data.

As an additional test, we fit the $Y_{\text{SZ}} - Y_X$ relation including a factor of $E(z)^C$, and fit for C while keeping the slope fixed to 1. We find $C = -0.36 \pm 0.58$, consistent with no evolution. Further investigating this, we divide the sample in two redshift bins. The low- z bin consists of the seven clusters at $z < 0.7$ while the high- z bin consists of the eight clusters at $z > 0.7$. Fixing the slope to 1, we find a ratio of 0.88 ± 0.12 for the low- z sample. For the high- z sample, we find a ratio of 0.72 ± 0.14 , offset by 1.4σ from the expected value. Excluding the most significant outlier, SPT-CL J0000-5748, improves the high- z sample’s agreement with the prediction by $\sim 0.8\sigma$, but does not significantly change the result. Overall, neither test finds statistically significant evidence for redshift evolution in the $Y_{\text{SZ}} - Y_X$ relation.

As discussed at the beginning of this section, the $Y_{\text{SZ},\text{sph}}/Y_X$ ratio is expected to be lower than 1 due to the different weighting of the temperature in the two estimates. As explained in Section 5.3, our measurement of Y_{SZ} is sensitive to the assumed temperature profile, whereas the Y_X measurement is not. This causes the measured $Y_{\text{SZ},\text{sph}}/Y_X$ ratio to change under different assumptions about the temperature profile. However, the expected ratio of the gas-mass-weighted and the spectroscopic-weighted temperatures changes by a similar amount as the temperature profile changes. The overall effect makes the measured ratio to be fairly independent to our assumptions of the shape of the temperature profile. This is particularly true for variations in the slope of the temperature profile at large radii that we tested in Section 5.3.

Overall we find a normalization marginally consistent with, although lower than, our expectations given the gas profiles in this work and believe this result to be largely independent of our assumed temperature profile. We find no significant evidence for a redshift-dependent evolution in the normalization of the $Y_{\text{SZ}} - Y_X$ relation, but note that the high- z sub-sample does favor a $\sim 1\sigma$ lower normalization. Additional X-ray and SZ observations of high- z clusters will be needed to make any statistically significant statements.

6.2.3. $Y_{\text{SZ}} - M_{500,Y_X}$ Relation

Finally, we investigate the relation between the SZ flux, Y_{SZ} , and the X-ray-derived mass, M_{500,Y_X} . This is not an independent

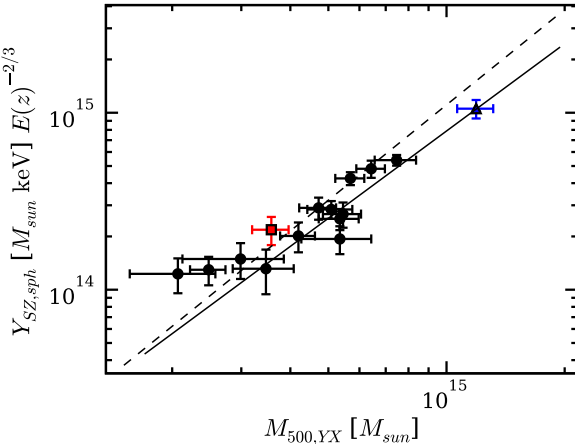


Figure 4. $Y_{\text{SZ}} - M_{500}$ relation for the sample. The plots show the $Y_{\text{SZ},\text{sph}}$ estimates, deprojected assuming a universal temperature profile. Masses are estimated from the M_{500,Y_X} relation. The dashed line shows the best-fit relation from Arnaud et al. (2010). SPT-CL J0551-5709 is shown as a red square and SPT-CL J0516-5430 is shown with a blue triangle.

result from the previous section because the X-ray masses are calculated directly from the Y_X measurements and the $M_{500,Y_X} - Y_X$ relation in Vikhlinin et al. (2009a). However, it is useful in understanding the SZ mass calibration and can be compared to previous measurements of this relation.

Using the method of Section 6.2.1, we fit a scaling relation between Y_{SZ} and M_{500,Y_X} of the form

$$Y_{\text{SZ}} = 10^A \left(\frac{M_{500,Y_X}}{3 \times 10^{14} M_\odot} \right)^B E(z)^{2/3} M_\odot \text{ keV}. \quad (19)$$

In Figure 4, we show the $Y_{\text{SZ}} - M_{500,Y_X}$ relation, and in Table 6 we give the best-fit parameters to Equation (19). The slope of this relation is found to be 1.67 ± 0.29 for $Y_{\text{SZ},\text{sph}} - M_{500,Y_X}$ with intrinsic scatter of 0.09 ± 0.05 (see Table 6). This slope is consistent with the self-similar expectation of $5/3$ and previous measurements (e.g., Bonamente et al. 2008; Arnaud et al. 2010). In Arnaud et al. (2010), a slope of 1.790 ± 0.015 is measured for their predicted $Y_{\text{SZ},\text{sph}}$ using X-ray observables.

We also fit the relation keeping the slope fixed at the value expected from X-ray studies, 1.79, and note that the normalization of the $Y_{\text{SZ}} - M$ relation is lower than that of Arnaud et al. (2010). The Arnaud et al. (2010) results imply a normalization $A = 14.115 \pm 0.003$, using our adopted h while we find $A = 14.03 \pm 0.04$, around a 2σ offset. The best-fit relation is shown in Figure 4 (solid line) with the Arnaud et al. (2010) relation shown (dashed line) for comparison.

It should be noted that part of the offset is due to differences in the mass estimates in our work and in the work of Arnaud et al. (2010). The normalization in the $M - Y_X$ relation (Equation (5)), used here to estimate cluster masses, is different from the normalization of the $M - Y_X$ relation used in Arnaud et al. (2010) to derive the $Y_{\text{SZ}} - M_{500,Y_X}$ relation in that work. For our adopted h , we find a mass, $M_{500,Y_X} = 4.83 \pm 0.17 \times 10^{14} M_\odot$, at $Y_X = 3 \times 10^{14} M_\odot \text{ keV}$ from Equation (5). If we instead use the $M - Y_X$ relation from Arnaud et al. (2010), we find $M_{500,Y_X} = 4.64 \pm 0.12 \times 10^{14} M_\odot$, at the same Y_X . To account for this scaling relation offset, we shift the normalization of the Arnaud et al. (2010) $Y_{\text{SZ}} - M_{500,Y_X}$ relation down by a factor $(4.83/4.64)^{1.79} = 1.074$, resulting in $A = 14.084 \pm 0.003$. This reduces the offset to our measurement, $A = 14.03 \pm 0.04$, to

a similar level to what we found for the $Y_{\text{SZ}} - Y_X$ relation in the previous section.

It is important to note that the intrinsic scatter in this scaling relation does not directly reflect the low scatter relationship between Y_{SZ} and the gravitational mass. The mass is derived directly from Y_X and therefore includes the scatter in the Y_X -mass relationship. Independent measurements of the gravitational mass, e.g., through weak lensing or hydrostatic masses from X-ray data, are necessary to diagnose scatter in the $Y_{\text{SZ}} - M$ relation.

7. CONCLUSIONS

We have presented the results from X-ray observations of a subset of 15 clusters from the first SZ-selected cluster catalog from the SPT cluster survey. We report the X-ray properties of this sample, including measurements of M_g , T_X , and Y_X , and have used T_X and Y_X to estimate the total masses of the clusters. We find generally good agreement between the X-ray properties of this sample and those expected from scaling relations of X-ray-selected samples. Separate from this result, we find a 3σ significant difference in the normalization of the $M_g - T_X$ relation when comparing the low- and high-redshift X-ray-selected samples from Vikhlinin et al. (2009a). This deviation from self-similar evolution could be indicative of an evolving gas mass fraction. However, the X-ray measurements of the SPT sample are not sensitive enough to confirm this.

Using the X-ray measured cluster positions and gas profiles, we have re-analyzed the SZ measurements to calculate each cluster's integrated Compton-y parameter, Y_{SZ} . We further use the X-ray measured gas profiles to deproject the SZ measurements so that they correspond to a spherical integrated Comptonization, $Y_{\text{SZ},\text{sph}}$, that is more directly comparable to the X-ray measurements.

We have calculated scaling relations between $Y_{\text{SZ},\text{sph}}$ and the X-ray measured quantities Y_X and M_{500,Y_X} . We fit the $Y_{\text{SZ},\text{sph}} - Y_X$ relation and find a slope consistent with unity, 0.96 ± 0.18 . Fixing this slope to 1, we re-fit the relation and find a normalization that implies a ratio of $Y_{\text{SZ},\text{sph}}/Y_X = 0.82 \pm 0.07$. This normalization effectively corresponds to the ratio between the mass-weighted and X-ray-spectroscopic-weighted temperature. For the spherically symmetric density and temperature profiles assumed in this work, we would have expected a ratio of 0.91 ± 0.01 , consistent with predictions from other X-ray studies of clusters (see, e.g., Vikhlinin et al. 2006; Arnaud et al. 2010). We therefore find a normalization of the $Y_{\text{SZ},\text{sph}} - Y_X$ relation that is marginally consistent with, although lower than, this prediction. This indicates that the SZ and X-ray measured pressure largely agree. We find no significant evolution in the $Y_{\text{SZ},\text{sph}} - Y_X$ relation. However, when considering a high- z sub-sample at $z > 0.7$, we find a ratio of 0.72 ± 0.14 , offset by 1.4σ from the expected value. Further X-ray and SZ observations of high-redshift clusters are needed to measure this ratio more accurately.

Using the Y_X measurement as a proxy for the total cluster mass with a relation calibrated in Vikhlinin et al. (2009a), we find similar results when we fit a $Y_{\text{SZ},\text{sph}} - M_{500,Y_X}$ relation. We find a slope consistent with the self-similar expectation of $Y_{\text{SZ}} \propto M^{5/3}$ and a normalization marginally consistent with the predictions from X-ray measurements by Arnaud et al. (2010). We have compared the Y_X inferred total mass to the SZ-significance-inferred total mass from Vanderlinde et al. (2010). Considering only the clusters used in their cosmological analysis, we find an average ratio of $M_{500,\text{SZ}}$ to M_{500,Y_X} of

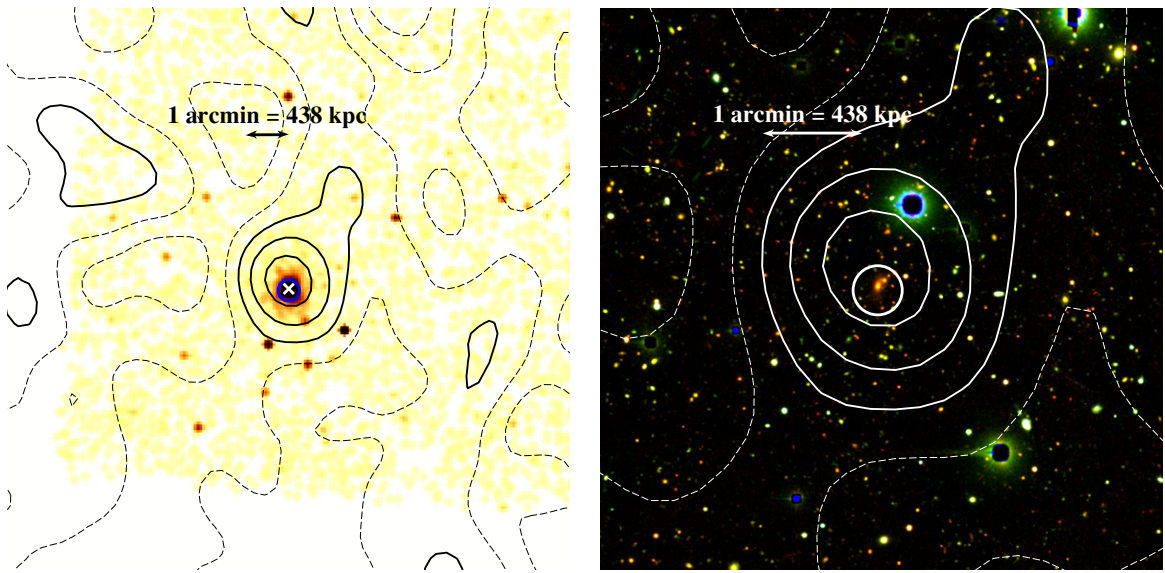


Figure 5. SPT-CL J0000-5748, $z = 0.74$. *Chandra* X-ray image (left) ($\sim 15' \times 15'$) in the 0.5–2.0 keV band is shown alongside an optical *grz*-image from the Magellan Baade 6.5 m telescope (right). Both X-ray and optical images are overlaid with SZ significance, ξ , contours from V10, spaced at 1.5σ increments starting from zero with dashed contours for $\xi \leq 0$ and solid contours for $\xi > 0$. The position of the BCG (B. Stalder et al., in preparation) is marked with a white cross in the X-ray images. The circle corresponds to the location of a SUMSS source as mentioned in the text. North is up and east is left.

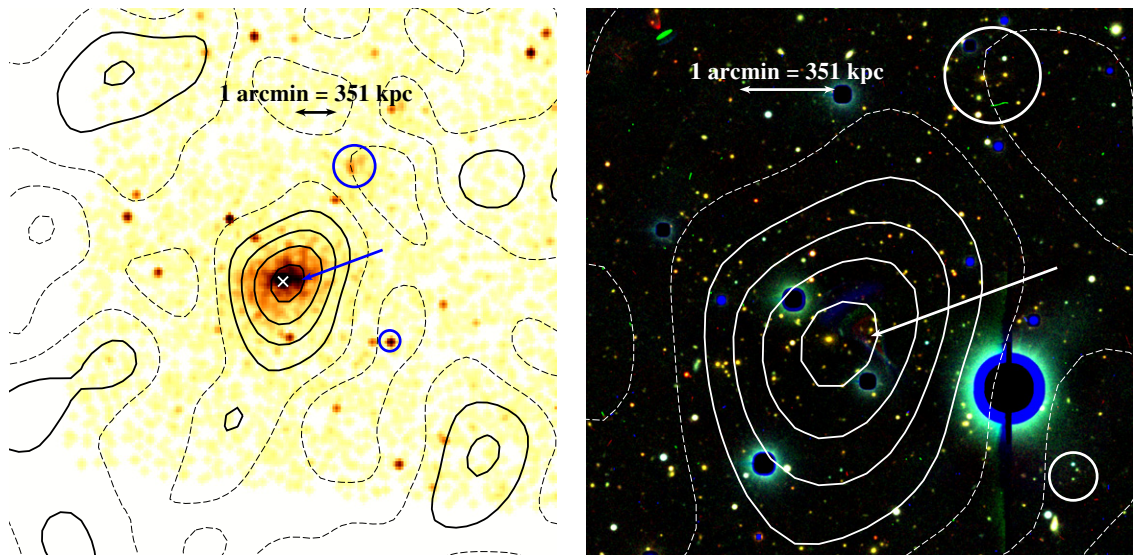


Figure 6. SPT-CL J0509-5342, $z = 0.4626$. *Chandra* X-ray image and Magellan *grz*-image. See Figure 5 for details. The large circle and arrow show the locations of interesting X-ray features, the small circle corresponds to the location of a SUMSS source as mentioned in the text.

0.78 ± 0.06 , a 1.3σ offset considering the $\sim 15\%$ systematic uncertainty on the simulation-based mass estimates in Vanderlinde et al. (2010).

This work is encouraging for future studies of SZ-selected clusters. The X-ray measurements confirm that the scaling relations of the SZ-selected clusters are consistent with the properties of other X-ray-selected samples of massive clusters. This result is important for the use of SZ-selected cluster samples to constrain cosmology and demonstrates that the X-ray measurements can play a valuable role in calibrating SZ surveys. This work also highlights the potential power of SZ surveys to study cluster evolution due to the broad redshift range of SZ-selected samples. As of 2011 January, the SPT has surveyed an additional $\sim 1300 \text{ deg}^2$ to a similar depth to the $\sim 178 \text{ deg}^2$ used in this work and expects to cover over 2500 deg^2 by

2011 December. These measurements will produce a catalog of hundreds of massive SZ-discovered clusters that extend to high redshift. Joint X-ray and SZ measurements of these clusters promise to place interesting constraints on cluster formation and gas physics for the most massive young clusters in the universe.

The South Pole Telescope is supported by the National Science Foundation through grant ANT-0638937. Partial support is also provided by the NSF Physics Frontier Center grant PHY-0114422 to the Kavli Institute of Cosmological Physics at the University of Chicago, the Kavli Foundation, and the Gordon and Betty Moore Foundation.

Support for X-ray analysis was provided by NASA through Chandra Award Number GO0-11143 issued by the Chandra

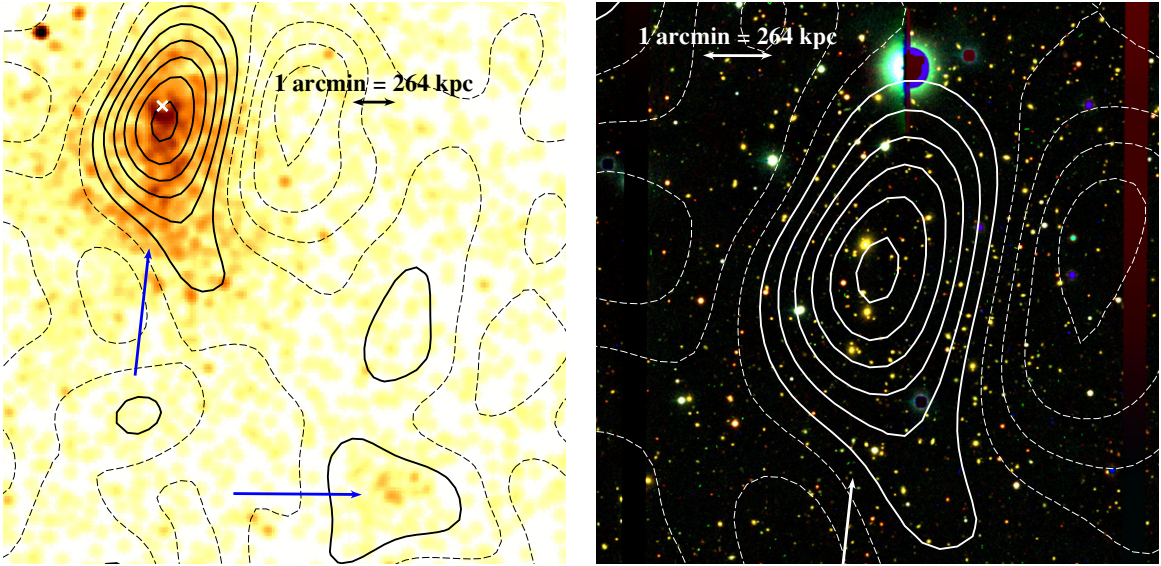


Figure 7. SPT-CL J0516-5430, $z = 0.2952$. *Chandra* X-ray image and Magellan *grz*-image. See Figure 5 for details. The arrows show the locations of interesting X-ray features, mentioned in the text.

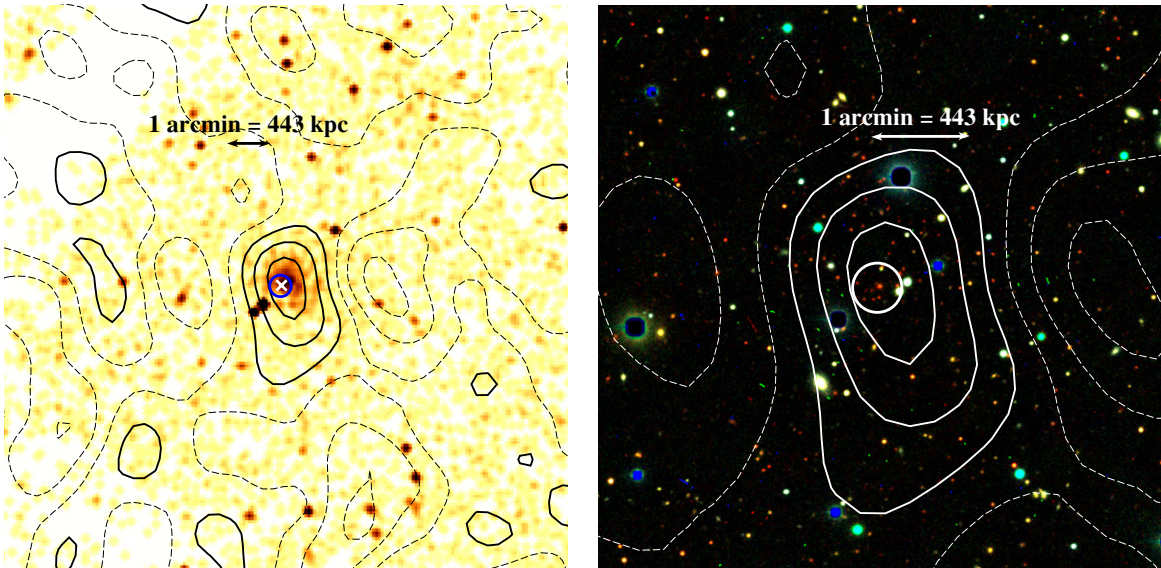


Figure 8. SPT-CL J0528-5300, $z = 0.7648$. *Chandra* X-ray image and Magellan *grz*-image. See Figure 5 for details. The circle shows the location of a SUMSS source, mentioned in the text.

X-ray Observatory Center, which is operated by the Smithsonian Astrophysical Observatory for and on behalf of NASA under contract NAS8-03060. Additional support is provided by NASA through XMM-Newton Award NNX09AQ04G and Chandra Award AR0-11015A. K. Andersson is supported in part by NASA through SAO Award Number 2834-MIT-SAO-4018 issued by the Chandra X-ray Observatory Center.

The Munich group is supported by the DFG through TRR33 “The Dark Universe” and the Excellence Cluster Universe. The McGill group acknowledges funding from the National Sciences and Engineering Research Council of Canada, the Quebec Fonds de recherche sur la nature et les technologies and the Canadian Institute for Advanced Research. The following individuals acknowledge additional support: B. Stalder from the Brinson Foundation, B. Benson from a KICP Fellowship, R. Foley from a Clay Fellowship, D. Marrone from Hubble Fellowship grant

HF-51259.01-A, N. W. Halverson acknowledges support from an Alfred P. Sloan Research Fellowship. M. Brodwin from the Keck Foundation, and A. T. Lee from the Miller Institute for Basic Research in Science, University of California Berkeley.

Facilities: CXO (ACIS), XMM (EPIC), Blanco (MOSAIC II), Magellan:Baade (IMACS), Magellan:Clay (LDSS2)

APPENDIX

NOTES ON INDIVIDUAL OBJECTS

In this section, we discuss the X-ray emission for each of the objects in the sample and note any extended substructures or other features in the X-ray images. Nearby radio sources as listed in the SUMSS survey are quoted with fluxes at 843 MHz, and we also discuss any particularly bright X-ray point sources. The

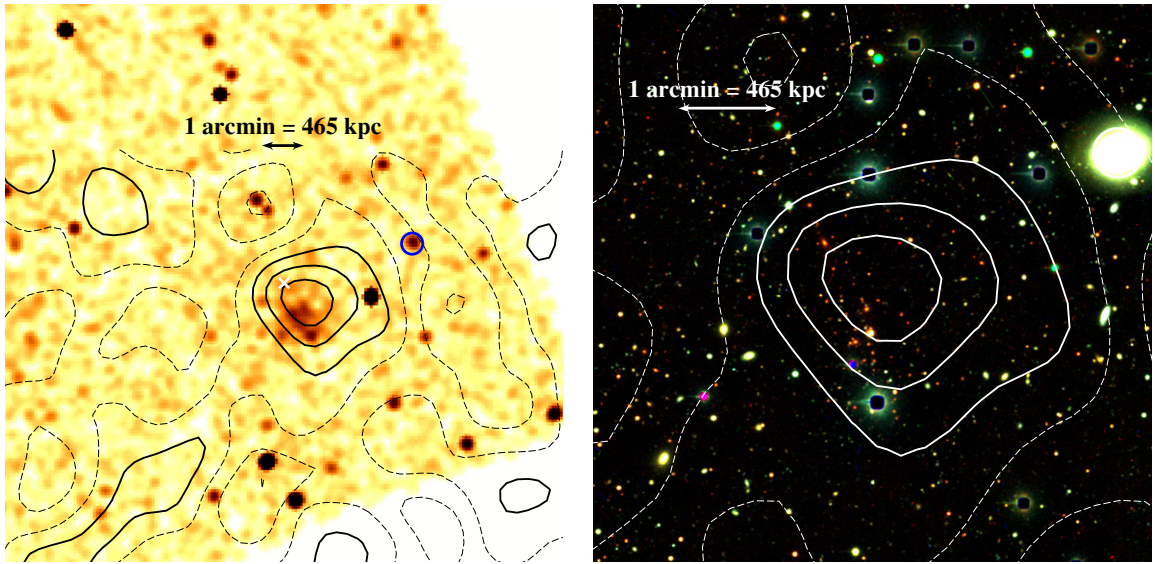


Figure 9. SPT-CL J0533-5005, $z = 0.8810$. *Chandra* X-ray image and Magellan *grz*-image. See Figure 5 for details. The circle shows the location of a SUMSS source, mentioned in the text.

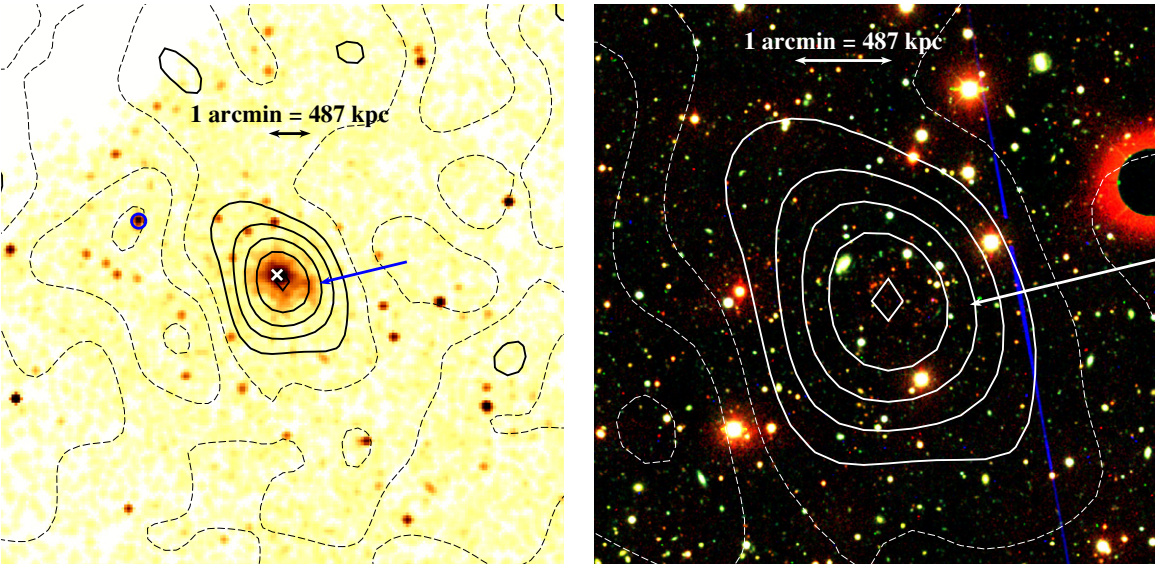


Figure 10. SPT-CL J0546-5345, $z = 1.0665$. *Chandra* X-ray image and BCS *grz*-image. See Figure 5 for details. The arrow shows the location of an X-ray substructure, discussed in the text. The small circle shows the location of a SUMSS source.

X-ray images ($\sim 15' \times 15'$) in the 0.5–2.0 keV band are shown in Figures 5–19 with optical *grz*-images from the Magellan Baade 6.5 m telescope (see High et al. 2010). For SPT-CL J0546-5345 and SPT-CL J2342-5411, we instead show *grz*-images from the BCS survey since Magellan images were not available in all filters for these objects. Both X-ray and optical images are overlaid with SZ significance, ξ , contours from V10. The contours are from spatially filtered SPT maps where the clusters appear as positive significance detections, and where the spatial filtering often causes noticeable negative significance ringing around the cluster. The contour levels are spaced at 1.5σ increments starting from zero with dashed contours for $\xi \leq 0$ and solid contours for $\xi > 0$. The position of the BCG (B. Stalder et al., in preparation) is marked with a white cross in the X-ray images. Large circles and arrows show the locations of interesting X-ray features, small circles correspond to locations of SUMSS sources mentioned in the text. North is up and east is left.

SPT-CL J0000-5748

This cluster is the highest redshift ($z = 0.74$) cluster in the sample with a sharp central brightness peak (see Figure 5). The X-ray peak is coincident with the BCG and is also associated with a SUMSS radio source with a flux of 40.4 ± 1.5 mJy indicative of a central AGN. The central brightness peak is broader than the *Chandra* PSF and we do not associate the central X-ray emission with AGN emission.

SPT-CL J0509-5342

There is a clear double peak in the central X-ray emission of this cluster (see Figure 6). The main peak is associated with the central BCG. The secondary peak is located $\sim 20''$ west of the main component (arrow) and the X-ray brightness ratio is 1/4. The secondary peak is also associated with two elliptical galaxies. The peak of the SZ flux is located between the two components.

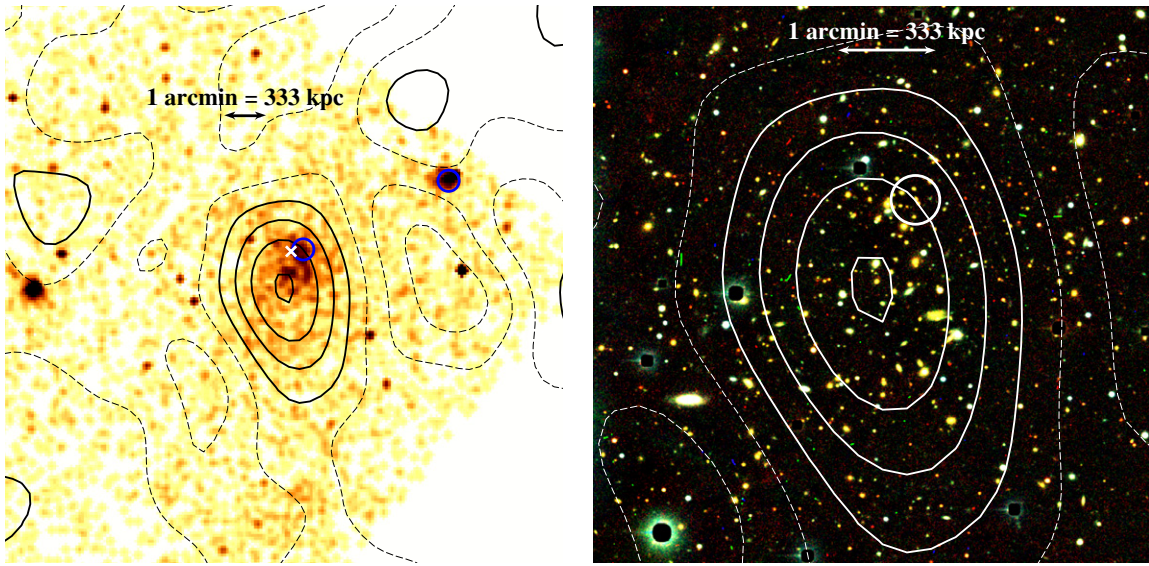


Figure 11. SPT-CL J0551-5709, $z = 0.4230$. *Chandra* X-ray image and Magellan *grz*-image. See Figure 5 for details. Circles correspond to locations of SUMSS sources mentioned in the text.

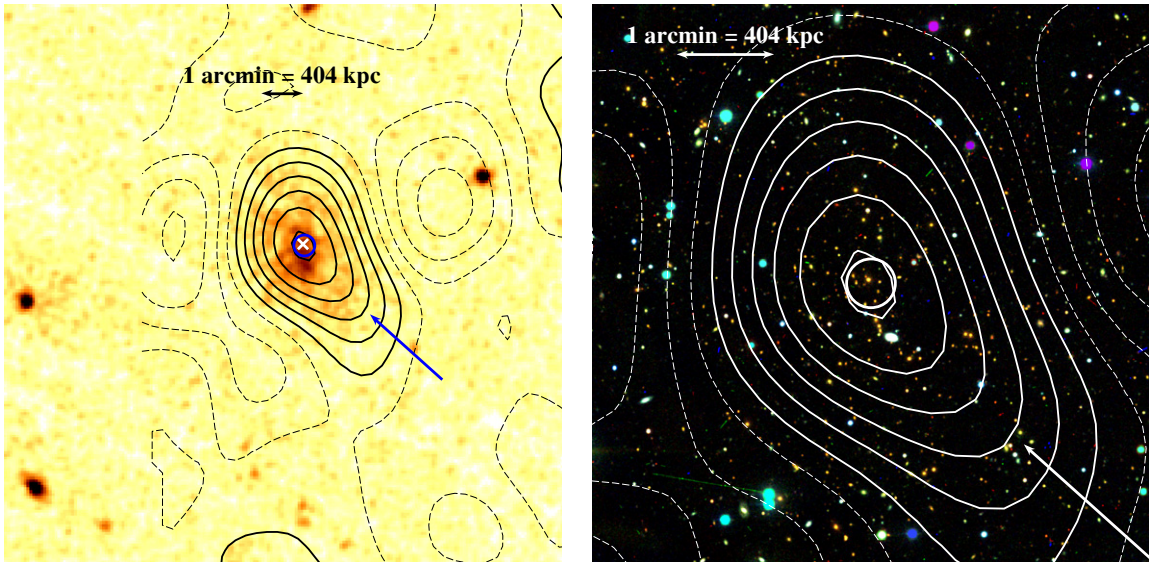


Figure 12. SPT-CL J0559-5249, $z = 0.6112$. *XMM-Newton* X-ray image and Magellan *grz*-image. See Figure 5 for details. The arrow shows an interesting X-ray feature, the circle corresponds to the location of a SUMSS source mentioned in the text.

The main component is the most centrally compact core in this sample which indicates that a possible merger is in an early stage. A bright SUMSS radio source with a flux of 125.7 mJy is located 2°SW of the cluster and is also coincident with an X-ray point source. This is not likely associated with the cluster. A possible third cluster component shows up as an extended X-ray source 3°NNW of the cluster (large circle) and is coincident with two elliptical galaxies in the optical image.

SPT-CL J0516-5430

This apparently merging cluster is very elongated along the N–S direction and also features a string of galaxies with the same alignment (see arrow in Figure 7). The BCG is also offset by 30'' from both the X-ray and SZ peaks. There is a second extended X-ray component 9°SW of the main cluster (SW arrow). This possible subcluster also shows up in the SZ map as an S/N > 2 detection. The subcluster is outside of the field of the

Magellan observation and no galaxy appears to be associated with this component in a Digitized Sky Survey image.

SPT-CL J0528-5300

This is a faint cluster ($L_X(0.5\text{--}2.0 \text{ keV}) = 1.9 \pm 0.210^{44} \text{ erg s}^{-1}$) without much structure and the BCG is offset by 15'' from the X-ray peak (Figure 8). The BCG is coincident with a SUMSS radio source with a flux of $61.2 \pm 2.0 \text{ mJy}$ likely associated with a central AGN.

SPT-CL J0533-5005

This is another faint cluster ($L_X(0.5\text{--}2.0 \text{ keV}) = 1.2 \pm 0.310^{44} \text{ erg s}^{-1}$) with no well-defined core. The BCG is offset 45'' from the central X-ray emission indicating an unrelaxed state (Figure 9). The SZ and X-ray peaks are also offset by 30''. A local galaxy at $z = 0.0147$ is located 3' NW of the cluster (circle) but is not likely to affect X-ray or SZ measurements.

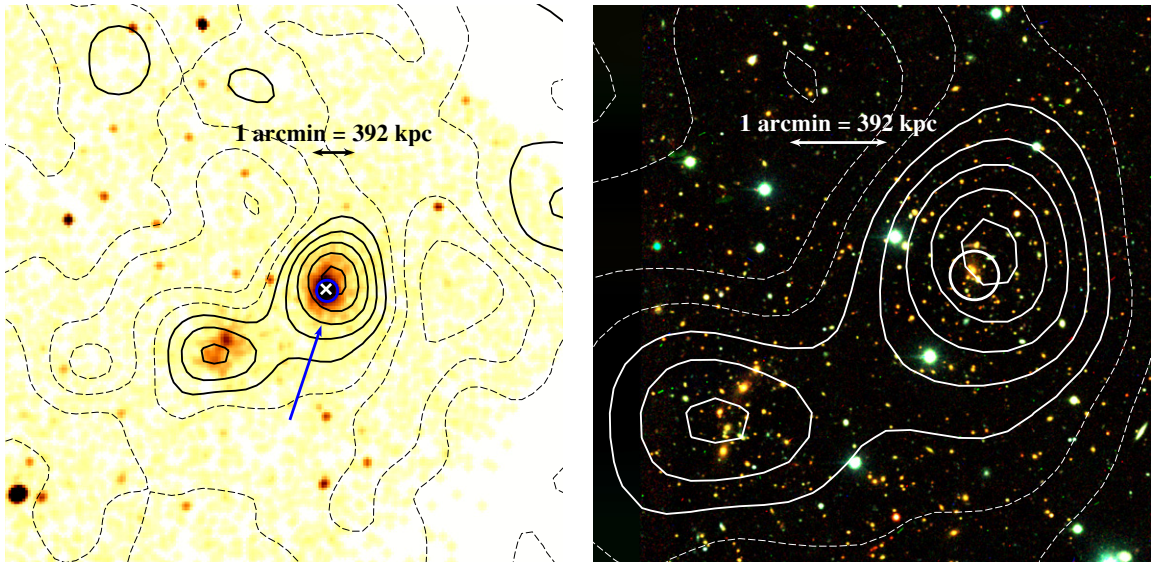


Figure 13. SPT-CL J2331-5051, $z = 0.5707$. *Chandra* X-ray image and Magellan *grz*-image. See Figure 5 for details. The arrow shows the location of an X-ray feature, see the text. The circle corresponds to a SUMSS source.

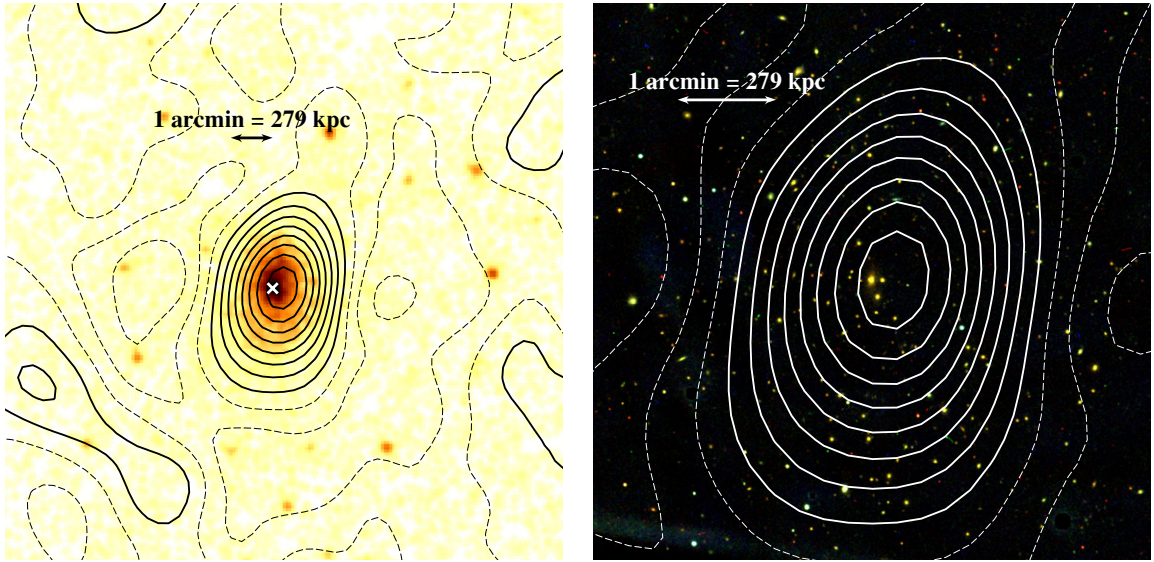


Figure 14. SPT-CL J2332-5358, $z = 0.32$. *XMM-Newton* X-ray image and Magellan *grz*-image. See Figure 5 for details.

SPT-CL J0546-5345

The X-ray image in Figure 10 shows a substructure extending $\sim 1'$ SW from the main cluster (arrow) suggesting that a minor merger may be taking place. This elongation is aligned with an apparent extension of the SZ signal further supporting this scenario. One of the X-ray point sources, $6'$ NW, is associated with a SUMSS radio source with a radio flux of 19.1 ± 0.9 mJy.

SPT-CL J0551-5709

This apparently merging cluster has a disturbed X-ray morphology and the X-ray and SZ peaks are offset by $30''$. A SUMSS radio source with flux of 22.7 ± 1.6 mJy is located $15''$ east of the BCG in a region with an overdensity of cluster galaxies (Figure 11). Another radio source is located $5'$ NE of the cluster and is associated with an X-ray source and a local galaxy.

The X-ray morphology and temperature structure of this object suggest that it is projected on top of a low-redshift

structure. Extended emission can be seen both toward the S and NW, covering a large area beyond r_{500} . The temperature decreases from 4.4 keV to 3.3 keV when increasing the aperture radius from $0.5 r_{500}$ to r_{500} , implying that this extended emission has very low temperature. The emission is likely associated with AS0552, located at this position. High et al. (2010) find a strong red sequence at $z = 0.09$ at the cluster location. The X-ray emission associated with this local cluster will likely bias any measurement of the temperature due to the contribution of the low- z flux at large radii. We attempt to correct for this bias as described in Section 3.5.

SPT-CL J0559-5249

The peak of the X-ray emission is offset to the south by $\sim 25''$ with respect to the BCG location and SZ peak in this cluster (Figure 12). The X-ray emission south of the BCG is associated with a group of galaxies at this location. The BCG is coincident with a 50.1 ± 2.7 mJy SUMSS radio source. On larger scales, the

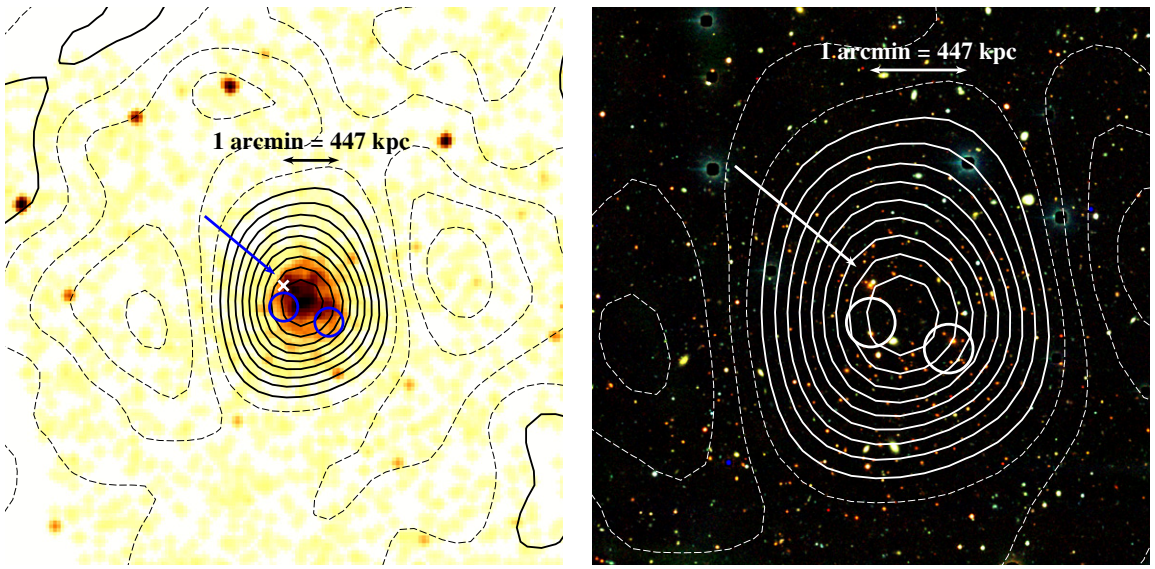


Figure 15. SPT-CL J2337-5942, $z = 0.7814$. *Chandra* X-ray image and Magellan *grz*-image. See Figure 5 for details. The arrow shows the location of a sharp surface brightness gradient. The circles correspond to the locations of SUMSS sources.

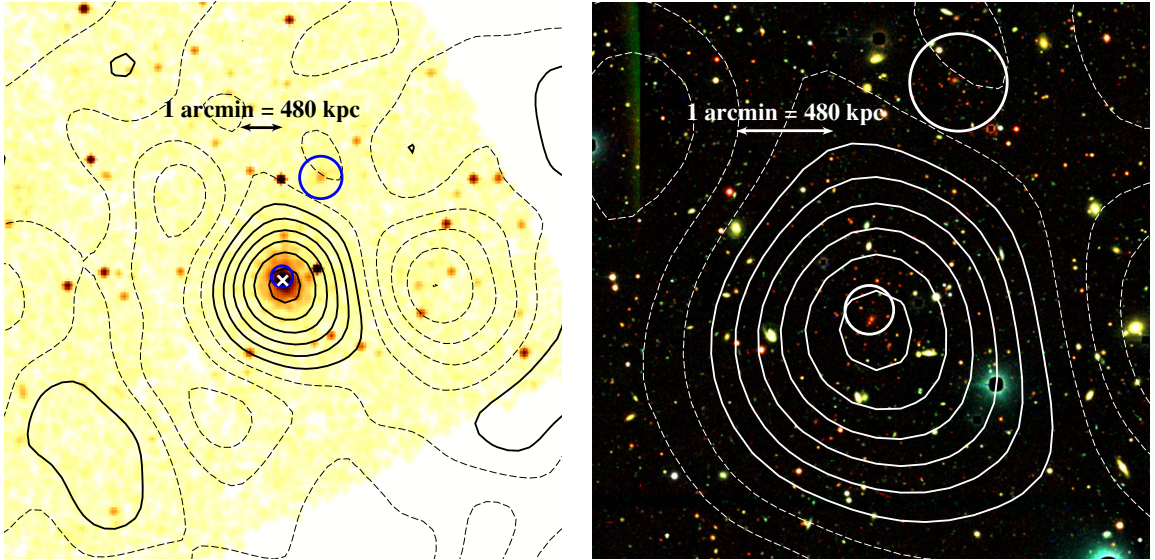


Figure 16. SPT-CL J2341-5119, $z = 0.9983$. *Chandra* X-ray image and Magellan *grz*-image. See Figure 5 for details. The large circle shows the location of a faint, extended X-ray source. The small circle corresponds to the location of a SUMSS source.

X-ray emission and SZ signal are extended to the SW, clearly visible 2/5 from the cluster core (arrow in Figure 12). This cluster is clearly in a merging state.

SPT-CL J2331-5051

As noted in V10, this cluster appears to be a pair of merging clusters with the smaller component located 2.5 SE of the main cluster. A spectral analysis of the smaller component indicates that it has a luminosity of 2×10^{43} erg s $^{-1}$, roughly 5% of the main cluster. As can be seen in Figure 13, the location of the X-ray emission and SZ decrement at the subcluster show very good agreement. This subcluster was also confirmed (see High et al. 2010) to be at the same redshift as the main cluster. Additionally, this cluster has a well-defined X-ray cavity 18'' S of the X-ray peak (arrow). This cluster also hosts a cool core, coincident with the BCG and a 13.3 ± 1.0 mJy SUMSS radio source.

SPT-CL J2332-5358

This nearby ($z = 0.32$) regular cluster shows no sign of significant structure in our *XMM-Newton* observation with 7 ks of good data. The location of the BCG, the X-ray peak, and the peak of the SZ signal show good agreement and the cluster is likely relaxed (see Figure 14). This cluster is also the only candidate in V10 with a point source detected in the SPT 220 GHz maps at $> 5\sigma$. We correct the SZ flux and position of the cluster by subtracting this source from the 150 GHz assuming a dust spectral index as described in Section 5.4.

SPT-CL J2337-5942

This cluster shows a sharp X-ray surface brightness discontinuity NE of the cluster center (arrow in Figure 15). Interestingly, the BCG is also located in this region, providing tentative evidence that this is a compact gas core moving through

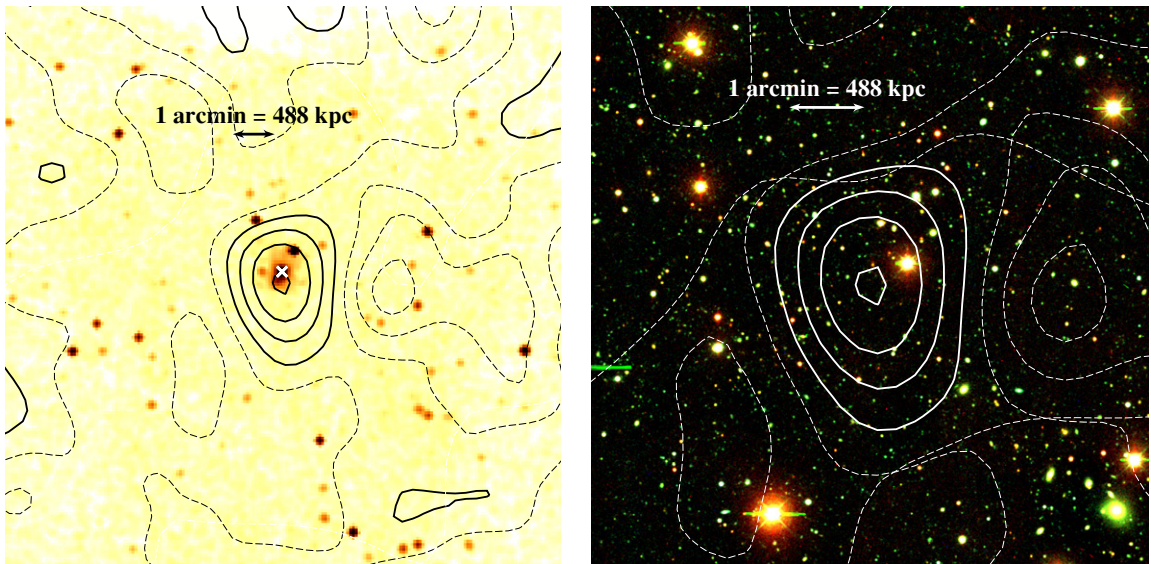


Figure 17. SPT-CL J2342-5411, $z = 1.08$. *Chandra* X-ray image and BCS grz -image. See Figure 5 for details.

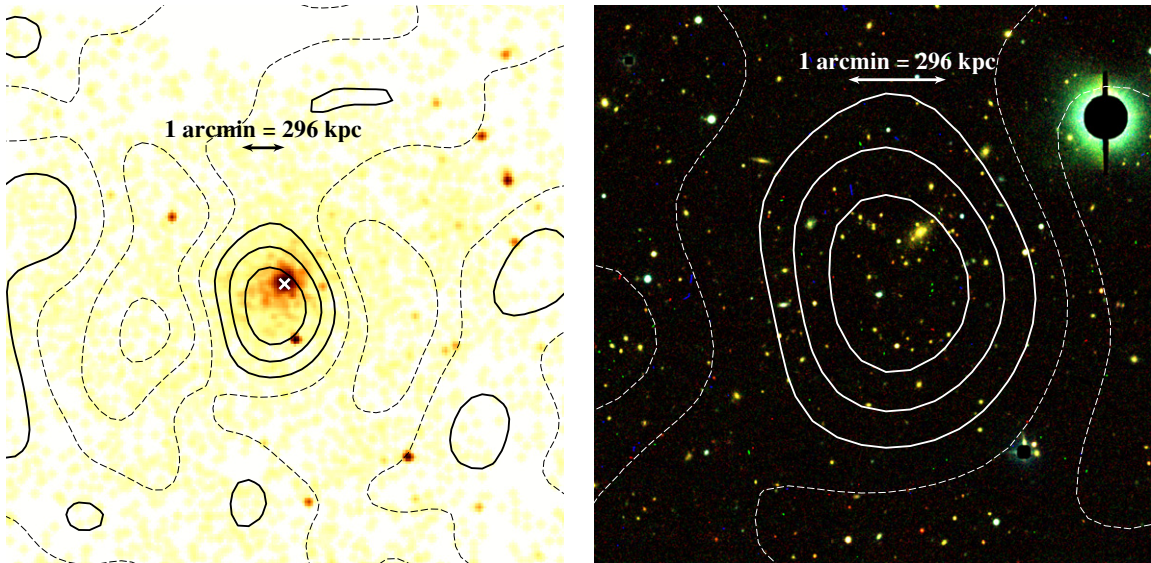


Figure 18. SPT-CL J2355-5056, $z = 0.35$. *Chandra* X-ray image and Magellan grz -image. See Figure 5 for details.

the ambient cluster medium, driving a shock front. The cluster shows an overall irregular morphology without a clear peak in the X-ray emission. This is the cluster with the highest SZ signal in the sample and is the second most massive with $M_{500,Y_X} = 7.43 \pm 0.80 \times 10^{14} M_\odot$. There are two SUMSS radio sources with 7.1 ± 1.0 mJy and 7.8 ± 1.0 mJy fluxes $33''$ and $23''$, respectively from the cluster center.

SPT-CL J2341-5119

In this cluster there are no signs of significant structure within the cluster in the X-ray data (see Figure 16). However, 2.5° NNW of the cluster center (large circle) there is a faint extended X-ray source at the location of a bright galaxy indicating that this is a satellite galaxy group about to merge with the main cluster. The BCG shows good correspondence with the X-ray peak and the main cluster appears relaxed. There is a 7.9 ± 1.1 mJy SUMSS radio source $6''$ N of the BCG which could be associated with a central AGN.

SPT-CL J2342-5411

This high-redshift ($z = 1.08$) cluster shows no signs of significant merger activity and is likely relaxed. However, there is a possible secondary component or tail to the SW, $15''$ from the core.

SPT-CL J2343-5521

In a 70 ks *Chandra* observation, no X-ray source was found at the location of this SPT detection ($\xi = 5.74$). This field was also imaged with BCS and Magellan with no optical counterpart found. The optical data suggested that this cluster would have to be at $z \gtrsim 1.2$ to not find an optical counterpart in either observation (High et al. 2010). The long *Chandra* observation allows us to put strict upper limits on the luminosity. Assuming that the cluster is at $z = 1$, the 5σ upper limit is $L_X(0.5\text{--}2.0\text{ keV}) < 3 \times 10^{42} \text{ erg s}^{-1}$. The same limit assuming $z = 2$ is $10^{43} \text{ erg s}^{-1}$. Additionally, no cluster counterparts could be identified in a $3.6 \mu\text{m}$ *Spitzer*/IRAC observation. The X-ray,

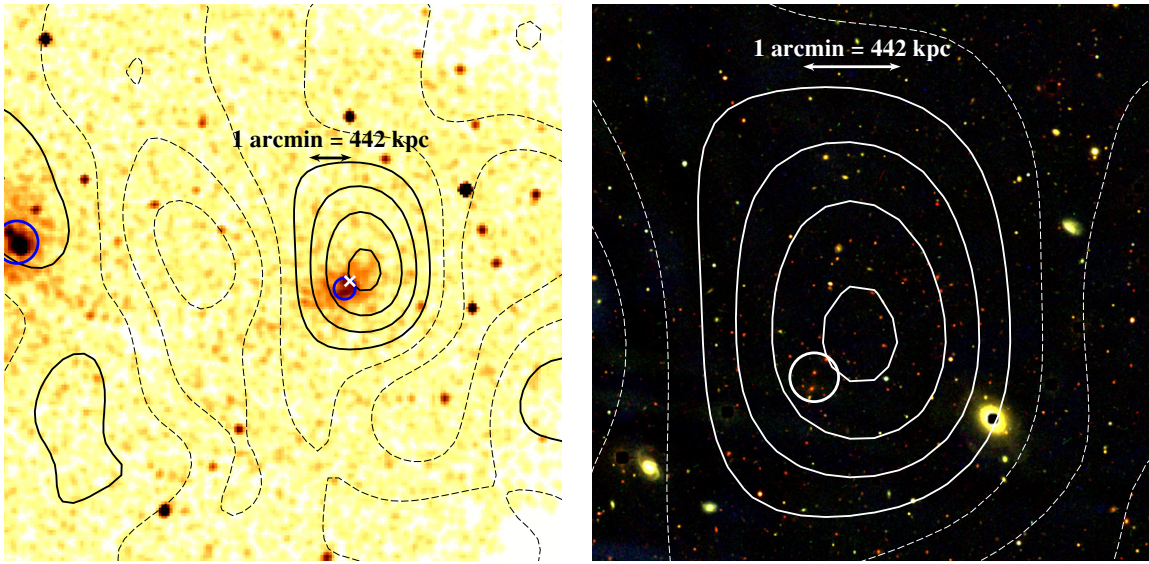


Figure 19. SPT-CL J2359-5009, $z = 0.76$. *Chandra* X-ray image and Magellan *grz*-image. See Figure 5 for details. The large circle shows the location of a local galaxy. The smaller circle shows the location of a SUMSS radio source.

IR, and optical data all strongly support that this is a single band false detection by SPT.

SPT-CL J2355-5056

This cluster shows good agreement between the position of the BCG and the X-ray peak and shows no significant structure in the X-ray image (Figure 18). The SZ peak is offset $\sim 35''$ to the south of the BCG while there is no evidence for extended X-ray emission in this direction. The X-ray emission is peaked in the center, likely due to a cool core.

SPT-CL J2359-5009

The X-ray image in Figure 19 reveals a $45''$ offset between the location of the SPT SZ detection and the X-ray peak. The BCG position is offset from the SZ peak by $33''$. Located east of the cluster is a local ($z = 0.029$) galaxy pair (circle, 7.5 E) which is clearly seen in both the X-ray and optical images. Another local galaxy ($z = 0.047$) is associated with a faint X-ray source (1.8 W), this is excluded from our X-ray analysis. A very bright point source is also visible in the X-ray image (3.5 NW), likely associated with an AGN. We do not find a counterpart to this source in the NASA/IPAC extragalactic database (NED) and estimate a flux of 1.6×10^{-13} erg s $^{-1}$ cm $^{-2}$ in the 0.5–2.0 keV band. A SUMSS radio source is located $15''$ SE of the BCG with a flux of 21 ± 1.1 mJy. The X-ray morphology is elongated along the east–west direction, possibly indicating merging activity. This is also supported by the ~ 70 kpc offset between the X-ray peak and the BCG position.

REFERENCES

- Akritas, M. G., & Bershady, M. A. 1996, *ApJ*, **470**, 706
 Anders, E., & Grevesse, N. 1989, *Geochim. Cosmochim. Acta*, **53**, 197
 Andersson, K. E., & Madejski, G. M. 2004, *ApJ*, **607**, 190
 Andersson, K., Peterson, J. R., Madejski, G., & Goobar, A. 2009, *ApJ*, **696**, 1029
 Arnaud, M., Pratt, G. W., Piffaretti, R., Böhringer, H., Croston, J. H., & Pointecouteau, E. 2010, *A&A*, **517**, A92
 Austermann, J. E., et al. 2010, *MNRAS*, **401**, 160
 Bautz, M. W., et al. 2009, *PASJ*, **61**, 1117
 Bode, P., Ostriker, J. P., Weller, J., & Shaw, L. 2007, *ApJ*, **663**, 139
 Böhringer, H., et al. 2004, *A&A*, **425**, 367
 Bonamente, M., Joy, M., LaRoque, S. J., Carlstrom, J. E., Nagai, D., & Marrone, D. P. 2008, *ApJ*, **675**, 106
 Brodwin, M., et al. 2010, *ApJ*, **721**, 90
 Carlstrom, J. E., Holder, G. P., & Reese, E. D. 2002, *ARA&A*, **40**, 643
 Carlstrom, J. E., et al. 2011, *PASP*, **123**, 568
 Coble, K., et al. 2007, *AJ*, **134**, 897
 Coppin, K., et al. 2006, *MNRAS*, **372**, 1621
 Devlin, M. J., et al. 2009, *Nature*, **458**, 737
 de Zotti, G., Ricci, R., Mesa, D., Silva, L., Mazzotta, P., Toffolatti, L., & González-Nuevo, J. 2005, *A&A*, **431**, 893
 Dressler, A., Hare, T., Bigelow, B. C., & Osip, D. J. 2006, *Proc. SPIE*, **6269**, 62690F
 Edge, A. C., & Stewart, G. C. 1991, *MNRAS*, **252**, 414
 Forman, W., et al. 2007, *ApJ*, **665**, 1057
 Fujita, Y., Tawa, N., Hayashida, K., Takizawa, M., Matsumoto, H., Okabe, N., & Reiprich, T. H. 2008, *PASJ*, **60**, 343
 George, M. R., Fabian, A. C., Sanders, J. S., Young, A. J., & Russell, H. R. 2009, *MNRAS*, **395**, 657
 Ghizzardi, S. 2001, XMM-SOC-CAL-TN-0022, available at <http://xmm.vilspa.esa.es>
 Haehnelt, M. G., & Tegmark, M. 1996, *MNRAS*, **279**, 545
 Haiman, Z., Mohr, J. J., & Holder, G. P. 2001, *ApJ*, **553**, 545
 Hall, N. R., et al. 2010, *ApJ*, **718**, 632
 High, F. W., et al. 2010, *ApJ*, **723**, 1736
 Hoshino, A., et al. 2010, *PASJ*, **62**, 371
 Itoh, N., Kohyama, Y., & Nozawa, S. 1998, *ApJ*, **502**, 7
 Jeltema, T. E., Hallman, E. J., Burns, J. O., & Motl, P. M. 2008, *ApJ*, **681**, 167
 Kalberla, P. M. W., Burton, W. B., Hartmann, D., Arnal, E. M., Bajaja, E., Morras, R., & Pöppel, W. G. L. 2005, *A&A*, **440**, 775
 Kelly, B. C. 2007, *ApJ*, **665**, 1489
 Komatsu, E., et al. 2011, *ApJS*, **192**, 18
 Kravtsov, A. V., Nagai, D., & Vikhlinin, A. A. 2005, *ApJ*, **625**, 588
 Kravtsov, A. V., Vikhlinin, A., & Nagai, D. 2006, *ApJ*, **650**, 128
 Lau, E. T., Kravtsov, A. V., & Nagai, D. 2009, *ApJ*, **705**, 1129
 Lima, M., Jain, B., & Devlin, M. 2010a, *MNRAS*, **406**, 2352
 Lima, M., Jain, B., Devlin, M., & Aguirre, J. 2010b, *ApJ*, **717**, L31
 Lin, Y.-T., Partridge, B., Poher, J. C., Bouchevry, K. E., Burke, S., Klein, J. N., Coish, J. W., & Huffenberger, K. M. 2009, *ApJ*, **694**, 992
 Lueker, M., et al. 2010, *ApJ*, **719**, 1045
 Mantz, A., Allen, S. W., Ebeling, H., Rapetti, D., & Drlica-Wagner, A. 2010, *MNRAS*, **406**, 1773
 Markevitch, M. 1998, *ApJ*, **504**, 27
 Marrone, D. P., et al. 2009, *ApJ*, **701**, L114
 Mason, B. S., et al. 2010, *ApJ*, **716**, 739
 Mauch, T., Murphy, T., Buttery, H. J., Curran, J., Hunstead, R. W., Piestrzynski, B., Robertson, J. G., & Sadler, E. M. 2003, *MNRAS*, **342**, 1117
 Maughan, B. J. 2007, *ApJ*, **668**, 772
 Maughan, B. J., et al. 2008, *MNRAS*, **387**, 998

- Mazzotta, P., Rasia, E., Moscardini, L., & Tormen, G. 2004, *MNRAS*, **354**, 10
 McInnes, R. N., Menanteau, F., Heavens, A. F., Hughes, J. P., Jimenez, R.,
 Massey, R., Simon, P., & Taylor, A. 2009, *MNRAS*, **399**, L84
 Melin, J.-B., Bartlett, J. G., & Delabrouille, J. 2006, *A&A*, **459**, 341
 Melin, J.-B., Bartlett, J. G., Delabrouille, J., Arnaud, M., Piffaretti, R., & Pratt,
 G. W. 2011, *A&A*, **525**, A139
 Menanteau, F., & Hughes, J. P. 2009, *ApJ*, **694**, L136
 Menanteau, F., et al. 2009, *ApJ*, **698**, 1221
 Menanteau, F., et al. 2010, *ApJS*, **191**, 340
 Meneghetti, M., Rasia, E., Merten, J., Bellagamba, F., Ettori, S., Mazzotta, P.,
 Dolag, K., & Marri, S. 2010, *A&A*, **514**, A93
 Mohr, J. J., Fabricant, D. G., & Geller, M. J. 1993, *ApJ*, **413**, 492
 Mohr, J. J., Mathiesen, B., & Evrard, A. E. 1999, *ApJ*, **517**, 627
 Mohr, J. J., et al. 2008, Proc. SPIE, 7016, 70160L
 Motl, P. M., Hallman, E. J., Burns, J. O., & Norman, M. L. 2005, *ApJ*, **623**, L63
 Mroczkowski, T., et al. 2009, *ApJ*, **694**, 1034
 Nagai, D. 2006, *ApJ*, **650**, 538
 Nagai, D., & Lau, E. T. 2011, *ApJ*, **731**, L10
 Nagai, D., Vikhlinin, A., & Kravtsov, A. V. 2007, *ApJ*, **655**, 98
 Ngeow, C. C., Mohr, J., Zenteno, A., Data Management, D., BCS, & SPT
 Collaborations. 2009, BAAS, **41**, 448.04
 Ngeow, C., et al. 2006, Proc. SPIE, 6270, 627023
 Nord, M., et al. 2009, *A&A*, **506**, 623
 Nozawa, S., Itoh, N., Kawana, Y., & Kohyama, Y. 2000, *ApJ*, **536**, 31
 Padin, S., et al. 2008, *Appl. Opt.*, **47**, 4418
 Percival, W. J., et al. 2010, *MNRAS*, **401**, 2148
 Plagge, T., et al. 2010, *ApJ*, **716**, 1118
 Pratt, G. W., Croston, J. H., Arnaud, M., & Böhringer, H. 2009, *A&A*, **498**, 361
 Reiprich, T. H., & Böhringer, H. 2002, *ApJ*, **567**, 716
 Reiprich, T. H., et al. 2009, *A&A*, **501**, 899
 Riess, A. G., et al. 2009, *ApJ*, **699**, 539
 Sehgal, N., Bode, P., Das, S., Hernandez-Monteagudo, C., Huffenberger, K.,
 Lin, Y.-T., Ostriker, J. P., & Trac, H. 2010, *ApJ*, **709**, 920
 Shaw, L. D., Nagai, D., Bhattacharya, S., & Lau, E. T. 2010, *ApJ*, **725**, 1452
 Shaw, L. D., Zahn, O., Holder, G. P., & Doré, O. 2009, *ApJ*, **702**, 368
 Shirokoff, E., et al. 2011, *ApJ*, **736**, 61
 Staniszewski, Z., et al. 2009, *ApJ*, **701**, 32
 Suhada, R., et al. 2010, *A&A*, **514**, L3
 Sun, M., Voit, G. M., Donahue, M., Jones, C., Forman, W., & Vikhlinin, A.
 2009, *ApJ*, **693**, 1142
 Sunyaev, R. A., & Zeldovich, Y. B. 1972, *Comments Astrophys. Space Phys.*,
 4, 173
 Vanderlinde, K., et al. 2010, *ApJ*, **722**, 1180 (V10)
 Vieira, J. D., et al. 2010, *ApJ*, **719**, 763
 Vikhlinin, A., Kravtsov, A., & Forman, W. 2006, *ApJ*, **640**, 691
 Vikhlinin, A., et al. 2009a, *ApJ*, **692**, 1033
 Vikhlinin, A., et al. 2009b, *ApJ*, **692**, 1060
 Wang, L., & Steinhardt, P. J. 1998, *ApJ*, **508**, 483
 Zenteno, A., et al. 2011, *ApJ*, **734**, 3
 Zhang, Y.-Y., Finoguenov, A., Böhringer, H., Kneib, J.-P., Smith, G. P., Kneissl,
 R., Okabe, N., & Dahle, H. 2008, *A&A*, **482**, 451
 Zhang, Y.-Y., et al. 2010, *ApJ*, **711**, 1033